Optimal Control of a PHEV Based on Backward-Looking Model Extended with Powertrain Transient Effects

Soldo, Jure; Cvok, Ivan; Deur, Joško

energies

MDPI

Article

Optimal Control of a PHEV Based on Backward-Looking Model Extended with Powertrain Transient Effects

Jure Soldo *, Ivan Cvok and Joško Deur

Faculty of Mechanical Engineering and Naval Architecture, University of Zagreb, 10000 Zagreb, Croatia
* Correspondence: jure.soldo@fsb.hr

Abstract: The paper proposes a power flow control strategy for a P2 parallel plug-in hybrid electric vehicle (PHEV) which takes into account torque and power losses related to engine-on and gear shift transients. An extended backward-looking (EXT-BWD) model is proposed to account for the transient losses, while the control strategy combines a rule-based controller with an equivalent consumption minimization strategy. To describe the transient losses, the EXT-BWD model includes additional state variables related to engine on/off flag and gear ratio in the previous time step. To establish a performance benchmark for control strategy verification, a dynamic programming-based control variable optimization framework is established based on the EXT-BWD model. The proposed control strategy is demonstrated to improve the fuel efficiency and drivability compared to the original control strategy while retaining comparable computational efficiency.

Keywords: plug-in hybrid electric vehicle; power flow management; control; dynamic programming; backward-looking model; shift control; transient phenomena

Citation: Soldo, J.; Cvok, I.; Deur, J. Optimal Control of a PHEV Based on Backward-Looking Model Extended with Powertrain Transient Effects. *Energies* **2022**, *15*, 8152. https://doi.org/10.3390/en15218152

Academic Editors: Raffaello Cozzolino and Daniele Chiappini

Received: 23 September 2022
Accepted: 27 October 2022
Published: 1 November 2022

1. Introduction

The powertrains of Hybrid Electric Vehicles (HEVs) and their plug-in counterparts (PHEVs) include multiple power sources, typically engine and one or more electric machines that can operate as motors or generators supplied by an electrochemical battery or an ultracapacitor. To fully exploit the fuel saving and greenhouse emission reduction potential of (P)HEVs, an optimal power flow control strategy is required for optimal coordination of propulsion machines and usage of energy storage. The control strategies should also ensure sustaining the battery state of charge (SoC).

Most commonly, the power flow control strategies proposed in literature are based on heuristically determined rules (so-called rule-based (RB) controller; [1,2]), equivalent consumption minimization strategy (ECMS) as an instantaneous control variable optimization method (see [3,4]), or combination of those two approaches [5]. The power flow control strategies usually rely on a quasi-static, backward-looking (BWD) powertrain model to determine appropriate control action. The BWD model simplifies the powertrain description through static kinematic relations while considering only the SoC dynamics, and it relies on driving cycle data (vehicle velocity, acceleration, and road grade time profiles) to determine the remaining powertrain variables in the backward manner (i.e., from wheels towards the engine and electric machines) [6]. An adaptive RB control strategy is proposed in [2] based on the insights gained by conducting control variable optimization using the BWD powertrain model. An instantaneous optimization strategy based on the Pontryagin's Minimum Principle is proposed in [3], where the BWD model is used to define the Hamiltonian cost function. Similarly, equivalent consumption minimization strategies (ECMS) presented in [4,5] rely on the BWD model to calculate the equivalent fuel consumption to be minimized. To further enhance the control performance, model predictive control (MPC) strategies are proposed in [7,8], where the BWD model is used to predict the powertrain behavior over a receding horizon.

The power flow control strategies may considerably underperform in terms of fuel economy and drivability when applied on more realistic, fully-dynamic, forward-looking powertrain models or on vehicles. This is due to uncaptured hybrid transmission transient losses and frequent gearshifts or operating mode switching [9–11]. For the same reason, control variable optimization results obtained by using the BWD powertrain model may not be deemed as a credible benchmark. The control strategy presented in [12] attempts to improve the drivability and indirectly reduce the powertrain transient losses by minimizing the number of gear shifts and engine on/off events in a parallel PHEV. The control strategy presented in [13] for a PHEV with series–parallel configuration considers the total energy cost of changing between respective operating modes thus avoiding frequent mode switching and improving drivability. To smooth out the engine transients and suppress the related losses, the ECMS presented in [14] for an extended range electric vehicle (EREV) introduces an additional term in the cost function which penalizes the engine speed difference between two consecutive sampling intervals. In [15], an ECMS is developed for a parallel PHEV, which minimizes additional fuel consumption during engine transient. Control strategy in [16] improves upon the gear shift performance of a parallel-type HEV with double clutch transmission thus improving both the driving comfort and energy efficiency. MPC strategies proposed in [17,18] for parallel PHEVs rely on more computationally demanding forward-looking (FWD) powertrain models which take into account the engine torque dynamics to optimally control engine torque and engine on-off status thus discouraging frequent engine switching. To account for the engine and main clutch transient losses, MPC-based control strategy proposed in [19] introduces an empirically determined fuel mass flow penalty map which is a function of engine speed change and main clutch status. In [20], a back-propagation neural network is used to approximate a FWD powertrain model of a parallel PHEV, thus implicitly accounting for transient losses within an MPC strategy. Although the approaches presented in [19,20] yield fuel economy improvements, they rely on black box data-driven model that requires properly formulated, exhaustive training. An ECMS designed for a parallel PHEV in [21] utilizes a BWD powertrain model where clutch and engine transient losses are described by a physical power loss model. However, the model does not consider the effects of transmission synchronizers losses, powertrain inertia, and low-level control dynamics. In addition, the model is not validated against a more precise FWD model.

The main contributions of this paper include: (i) building a computationally efficient BWD model of a parallel PHEV powertrain, which takes into account all relevant effects of engine-on and gear shift transients to total fuel and electric energy consumption, and which is validated against a detailed FWD model, and (ii) designing a RB+ECMS power flow controller that takes into account the relevant engine-on and gear shift transient effects for improved fuel economy and drivability.

The remaining part of this paper is organized as follows. Section 2 describes the conventional BWD model and the detailed FWD model for a PHEV-type city bus. The RB+ECMS-type high-level controller and the low-level control system are presented in Section 3. The backward model extended with engine-on and shift transient losses (EXT-BWD model) is introduced in Section 4. DP-based control variable optimization formulation based on the EXT-BWD model is presented in Section 5, along with the optimization results given in support of EXT-BWD model validation. Verification of the proposed RB+ECMS controller based on the EXT-BWD model is conducted in Section 6 with respect to DP benchmark and the conventional RB+ECMS controller. Concluding remarks are given in Section 7.

2. Powertrain Models

2.1. Powertrain Configuration

A rear-wheel drive powertrain configuration of the considered parallel PHEV-type city bus (based on Volvo 7900 Electric Hybrid, [22]) is shown schematically in Figure 1. The main clutch separates a compression ignition internal combustion engine (ICE) from the rest

of powertrain, and it is disengaged when the engine is switched off. The motor/generator (M/G) machine supplied by a Li-Ion battery is placed between the main clutch and a 12-speed automated manual transmission (AMT). Finally, the power is transmitted to the rear wheels through a final drive gearbox and differential.

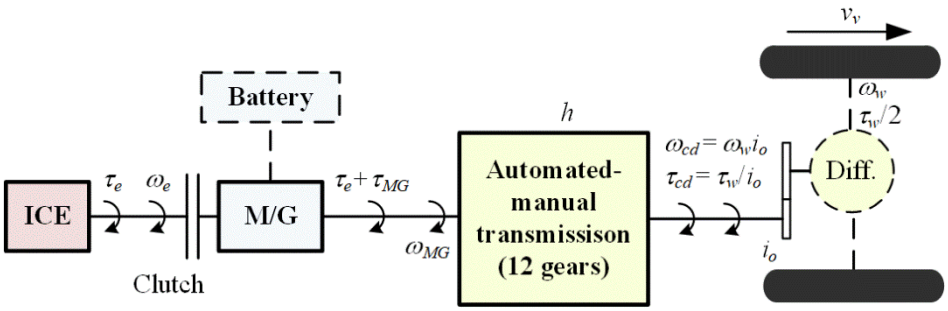

Figure 1. P2 Parallel PHEV powertrain configuration.

The AMT contains three reduction stages to achieve 12 gear ratios [10] (see schematic in Figure 2 and Table 1). The splitter gear stage (gears s_1 and s_2) is placed between the input shaft, which rotates at the speed ω_{MG}, and a counter-shaft that rotates at the speed ω_{cs} and transmits the torque τ_{ss} when engaged by synchronizers. The main gear reduction stage (gears m_1, m_2, and m_3) is placed between the main shaft rotating at the speed ω_{ms} and the counter-shaft, and it contains two dog clutches to achieve different gears. Note that if the gears s_2 and m_3 are engaged at the same time, the input and main shaft are directly connected (see Table 1 and Figure 2). Changing the main reduction gear requires the use of M/G machine to synchronize the speeds of target m-gear and main shaft. Note that the main gear reduction stage also comprises the reverse gear m_0 (not considered in this paper). Finally, the range gear reduction stage (gears r_1 and r_2) comprises a planetary gear set in which the ring gear can be synchronized via torque τ_{sr} of synchronizer r to the casing (gear r_1) or the carrier connected to the output shaft rotating at the speed ω_{os} (gear r_2). The gears are changed by controlling the positions of synchronizers and dog clutches through pneumatic actuators. Synchronizer and dog clutch normalized position values are denoted as s_{ps} and s_{pr} for synchronizers s and r, respectively, and s_{pm} for dog clutches. The list of 12 forward-gear indexes h_{idx}, the corresponding gear ratios h and normalized synchronizers positions are given in Table 1.

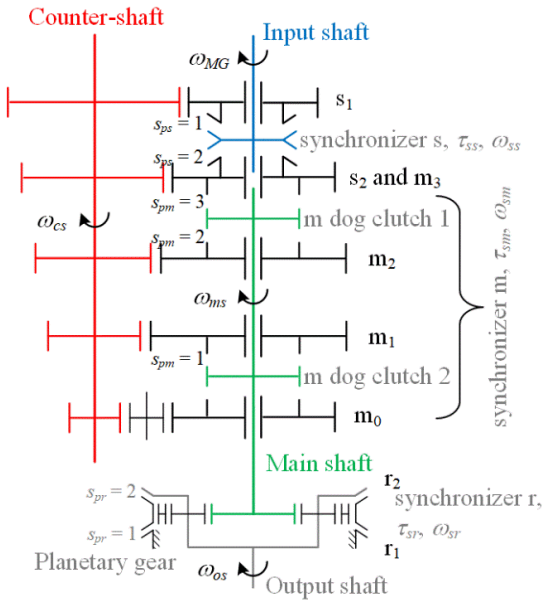

Figure 2. Schematics of 12-gear AMT.

Table 1. Gear shifting table of considered 12-speed AMT.

Gear h_{idx} [-]	Ratio h [-]	s_1	s_2	m_1	m_2	m_3	r_1	r_2	s_{ps}	s_{pm}	s_{pr}
1	14.94	x		x			x		1	1	1
2	11.73		x	x			x		2	1	1
3	9.04	x			x		x		1	2	1
4	7.09		x		x		x		2	2	1
5	5.54	x				x	x		1	3	1
6	4.35		x			x	x		2	3	1
7	3.44	x		x				x	1	1	2
8	2.70		x	x				x	2	1	2
9	2.08	x			x			x	1	2	2
10	1.63		x		x			x	2	2	2
11	1.27	x				x		x	1	3	2
12	1.00		x			x		x	2	3	2

2.2. Backward-Looking Powertrain Model

The backward-looking (BWD) model describes the kinematic relations between powertrain components, and the only state variable corresponds to the battery state-of-charge (SoC). In order to follow the specified driving cycle defined by the vehicle velocity time profile $v_v(t)$, the required wheel torque $\tau_w(t)$ is determined from the vehicle longitudinal dynamics equation as follows:

$$\tau_w = r_w M_v \dot{v}_v + r_w R_0 M_v g \cos(\delta_r) + r_w M_v g \sin(\delta_r) + 0.5 r_w \rho_{air} A_f C_d v_v^2, \quad (1)$$

where r_w is the effective tire radius, M_v is the vehicle mass, R_0 is the rolling resistance coefficient, g is the gravitational acceleration constant, δ_r is the road grade, ρ_{air} is the air density, A_f is the vehicle frontal area, and C_d is the aerodynamical drag coefficient. For the case of closed main clutch, the speeds of engine (ω_e), M/G machine (ω_{MG}), wheels (ω_w), and vehicle (v_v) are connected through the following equation (Figure 1):

$$\omega_{MG} = \omega_e = i_o h \omega_w = i_o h \frac{v_v}{r_w}, \quad (2)$$

where i_o is the final drive ratio and h is the transmission gear ratio. Similarly, in case of locked main clutch the transmission input shaft torque, i.e., the sum of M/G machine and engine torques, τ_{MG} and τ_e, respectively, is determined from the total wheel torque τ_w while accounting for the transmission ratio and mechanical power loss:

$$\tau_e + \tau_{MG} = \frac{\tau_w \eta_{tr}^{k_t}(\tau_w) + \frac{P_0(\omega_w)}{\omega_w}}{i_o h}, \quad (3)$$

where the coefficient k_t equals 1 for $\tau_w < 0$ (regenerative braking), and $k_t = -1$ holds for $\tau_w > 0$ (traction), η_{tr} is the torque-dependent transmission efficiency, and P_0 is the transmission speed-dependent power loss (see [23] for details). Note that in case of pure electric driving, ω_e = 0 rad/s and τ_e = 0 Nm hold. The model parameters are given in Appendix A.

The M/G machine efficiency map η_{MG} (τ_{MG}, ω_{MG}) and the engine specific fuel consumption map $A_{ek}(\tau_e, \omega_e)$ are shown in Figure 3, along with the corresponding maximum torque curves. These maps are adopted from the respective maps published in the literature for similar engine and M/G machine and are scaled with respect to maximum speed and

power ratios of the respective vehicles and the particular PHEV-type bus considered in this paper [20]. The map $A_{ek}(\tau_e, \omega_e)$ is used to calculate the fuel mass flow

$$\dot{m}_f = A_{ek}(\tau_e, \omega_e)\tau_e\omega_e, \tag{4}$$

which is then integrated to obtain the cumulative fuel consumption

$$V_f = \frac{1}{\rho_{fuel}} \int_{t=0}^{t_f} \dot{m}_f dt, \tag{5}$$

where ρ_{fuel} is the diesel fuel density.

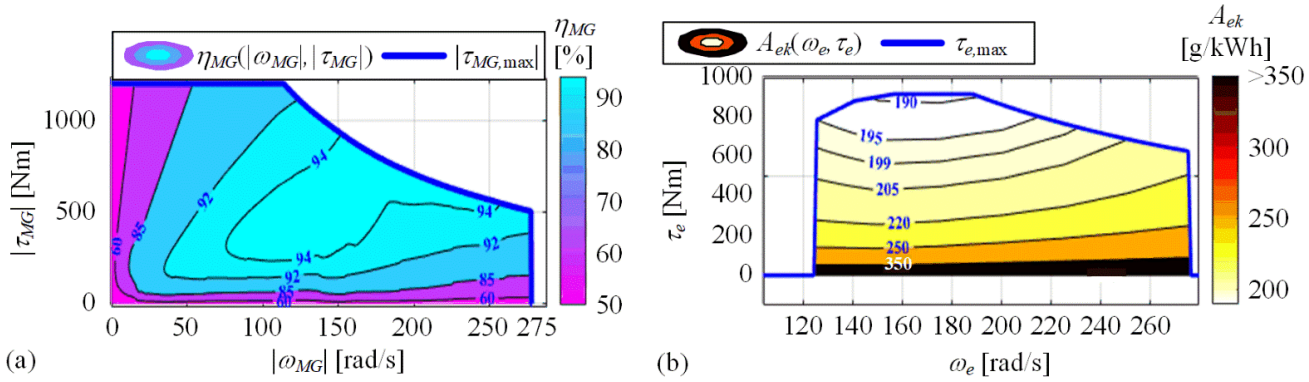

Figure 3. M/G machine (**a**) and engine maps (**b**).

The battery SoC is defined as $SoC = Q/Q_{\max}$, where Q and $Q_{\max}$ are actual and maximum battery charge, respectively. The SoC dynamics description is based on the equivalent battery circuit model illustrated in Figure 4a [6]:

$$\dot{SoC} = \frac{\sqrt{U_{oc}^2(SoC) - 4R(SoC)P_{batt}} - U_{oc}(SoC)}{2Q_{\max}R(SoC)}. \tag{6}$$

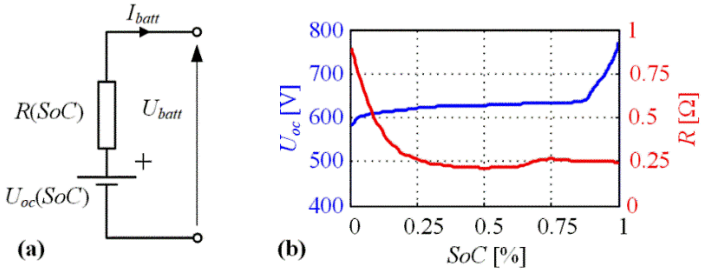

Figure 4. Equivalent circuit model (**a**) and SoC-dependent open-circuit voltage U_{oc} and internal resistance R (**b**) for LiFePO4 battery, reprinted with permission from [23].

The SoC-dependent open circuit voltage $U_{oc}(SoC)$ and the internal resistance $R(SoC)$ characteristics are given in Figure 4b [23]. The battery output power P_{batt} is expressed as follows:

$$P_{batt} = \eta_{MG}^{k_b}(|\tau_{MG}|, \omega_{MG})\tau_{MG}\omega_{MG}, \tag{7}$$

where $k_b = 1$ holds for regenerative braking ($\tau_{MG}\omega_{MG} < 0$) and $k_b = -1$ is valid for traction ($\tau_{MG}\omega_{MG} \geq 0$). The BWD model given by (1)–(7) is discretized and implemented in the Matlab/Simulink environment with the sampling time $T_d = 1$ s as a good trade-off between the computational efficiency and ability to capture the longitudinal dynamic transients [6].

2.3. Forward-Looking Powertrain Model

The forward-looking (FWD) model describes dominant dynamics of powertrain components including engine, M/G machine, and shaft inertias, output shaft compliance,

and transmission actuators. The FWD model is implemented in the Simcenter Amesim simulation environment, where proper physical models are selected for each powertrain component and then parameterized and combined into the overall powertrain model shown in Figures 5 and 6. The model contains 10 inertia elements, which include the engine inertia I_e, the lumped M/G machine and input shaft inertia I_{MG1}, the counter-shaft inertia I_{cs}, the main shaft inertia I_{ms}, the output shaft inertia I_{os}, the four wheel inertia $I_{w1} = I_{w2} = I_{w3} = I_{w4} = I_w$, and the vehicle mass M_v. The main model parameters can be found in [10]. The Amesim-embedded variable integration step solver is used in simulation [24].

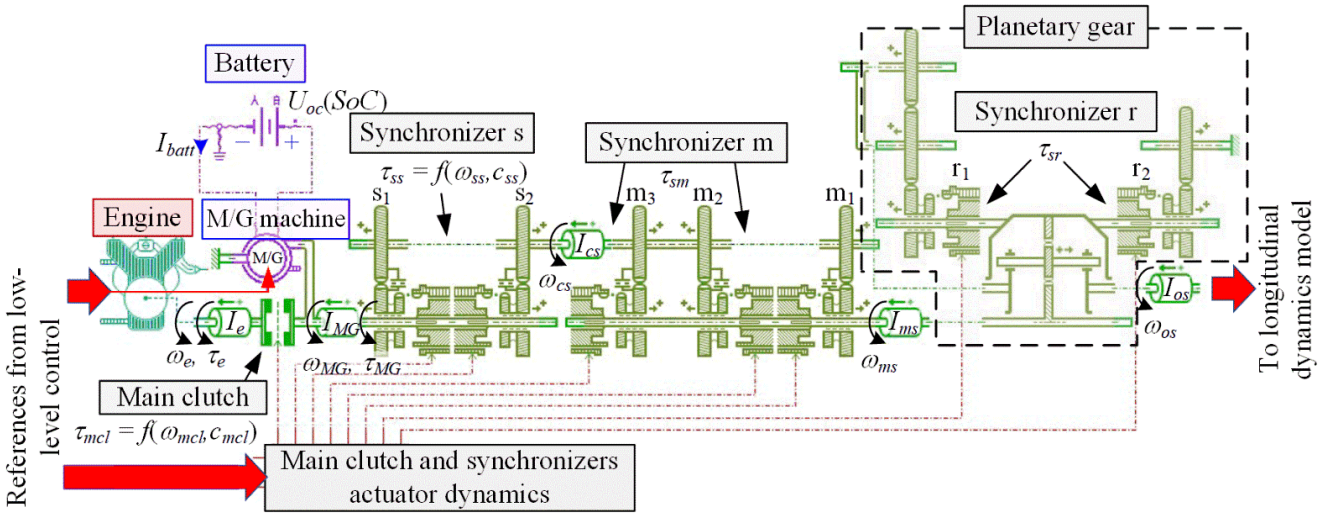

Figure 5. FWD model of PHEV powertrain implemented within Amesim.

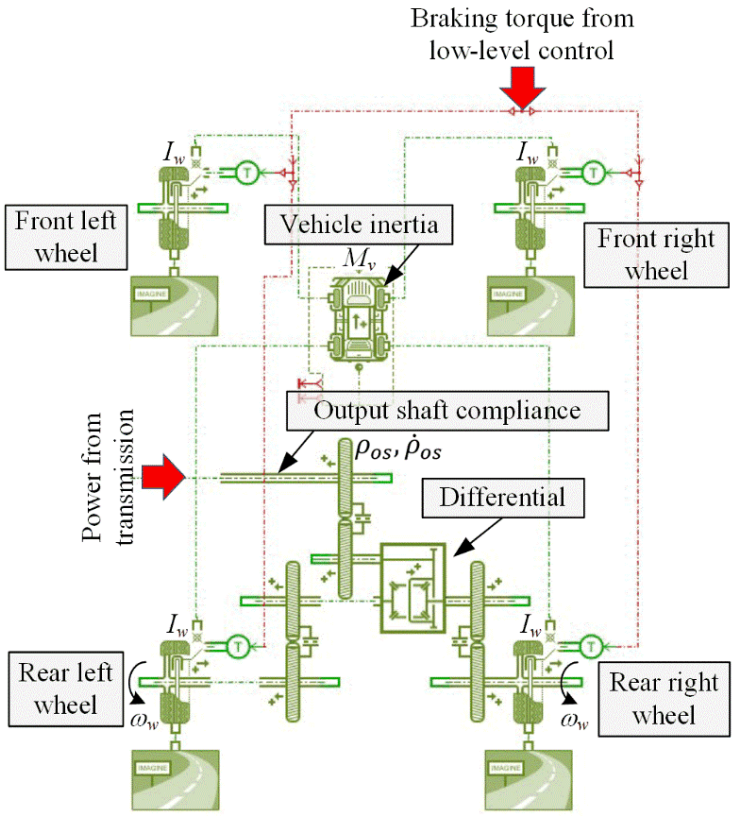

Figure 6. Driveline and longitudinal dynamics model implemented in Amesim.

The battery dynamics model is implemented based on Equations (6) and (7). Similarly, the M/G machine and engine maps shown in Figure 3 for BWD model are used in the FWD model as well. The M/G machine torque dynamics are modeled by the first-order lag term with the time constant T_{MG} = 10 ms, whereas the turbocharged Diesel engine torque dynamics are modeled by a first-order lag term with a speed dependent time constant $T_e(\omega_e)$ in the case of torque increase (see Figure 7b), and the fixed time constant of 10 ms in the case of torque decrease. The engine drag torque characteristic $\tau_{e,drag}(\omega_e)$ given in Figure 7a is applied when the engine is switched off.

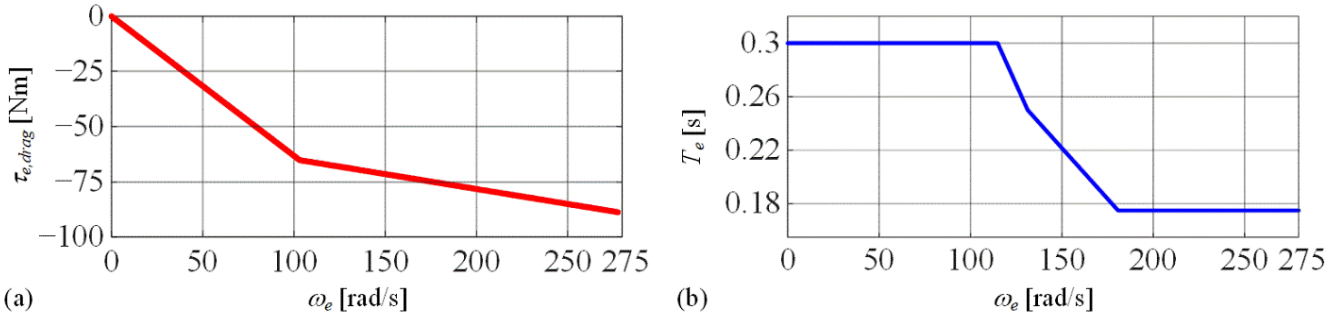

Figure 7. Engine drag torque characteristic (**a**) and turbocharged Diesel engine torque development time constant (**b**).

The main clutch friction torque τ_{mcl} is modelled by the classical Coulomb-type friction model, where the friction torque magnitude is proportional to the normalized clutch torque capacity c_{mcl} (ranging from 0 to 1 for open and lock clutch states, respectively). For the sake of model implementation simplicity, two dog clutch models are replaced by a synchronizer model for engaging gears m_1 and m_2, and a half-synchronizer model for engaging gear m_3. During the synchronization, the synchronizer torques τ_{ss}, τ_{sm}, and τ_{sr} are determined by a dynamic Coulomb-type friction model, where the torque magnitude is proportional to the normalized torque capacity (c_{ss}, c_{sm} and c_{sr}) dependent on the normalized synchronizer positions (s_{ps}, s_{pm} and s_{pr}), and where the stiction torque is modeled by a parallel spring-damper element [10].

The dynamics of main clutch pneumatic actuator are modeled by the first-order lag term with the time constant of 50 ms. The normalized synchronizer positions s_{ps}, s_{pm}, and s_{pr} assume values depending on the gear ratio h, as designated in Table 1. To account for the synchronizer pneumatic actuators dynamics, the synchronizer position dynamics are also modelled by the first-order lag term with the time constant of 20 ms.

The mechanical losses are modeled for each gear pair, and they are parametrized by using an Amesim's built-in tool [24]. The compliance of the rear-drive propulsion half-shafts is replaced by an equivalent compliance of the output shaft (Figure 6). A simplified Pacejka model is used to model the tire longitudinal force [25]. The vehicle weight distribution is simplified in terms of making it constant and equal for all four wheels throughout the trip. Finally, the total mechanical brake torque τ_{brk} is modeled by the first-order lag term with the time constant of 10 ms to account for the pneumatic actuator dynamics. Equal braking torque distribution on all four wheels is assumed.

3. Control Strategy

3.1. Structure of Overall Control Strategy

The overall powertrain control structure is illustrated in Figure 8, and it consists of a driver model, and high- and low-level control strategies. The driver is modelled as a proportional-integral (PI) vehicle speed controller, and it sets the wheel torque demand τ_{wd} for the high-level control strategy. The driver model parameters K_{Dr} and T_{Dr} are determined based on the damping optimum method for the target damping ratio ζ = 0.45 and the equivalent time constant T_{eq} = 0.75 s [26]. The driver wheel torque demand τ_{wd} is saturated with respect to maximum wheel torque characteristic determined by the engine

and M/G machine maximum torque curves given in Figure 3 and the drivetrain gear ratios h and i_0. Depending on the current values of wheel speed ω_w and battery SoC, the high-level control strategy transforms the wheel torque demand τ_{wd} to the low-level control strategy references, i.e., the transmission gear ratio h_R and the engine torque reference τ_{eR}, as well as the target engine on/off status flag EN_{stR}. The low-level control strategy is fed by the driver wheel torque demand τ_{wd} and the engine torque reference τ_{eR}, the current wheel, engine and M/G machine speeds (ω_w, ω_e, and ω_{MG}), and the current gear ratio h_R, and it outputs the main clutch torque capacity reference c_{mclR}, the synchronizer normalized position references (s_{psR}, s_{pmR} and s_{prR}), the M/G machine torque reference τ_{MGR}, the mechanical brake torque reference τ_{brkR}, and the engine torque reference τ^*_{eR} that may differ from high-level controller-commanded reference τ_{eR} in the case of transients (Section 3.3). The braking torque reference τ_{brkR} is determined by the low-level controller as the excess of driver brake torque with respect to M/G machine regenerative braking torque limit.

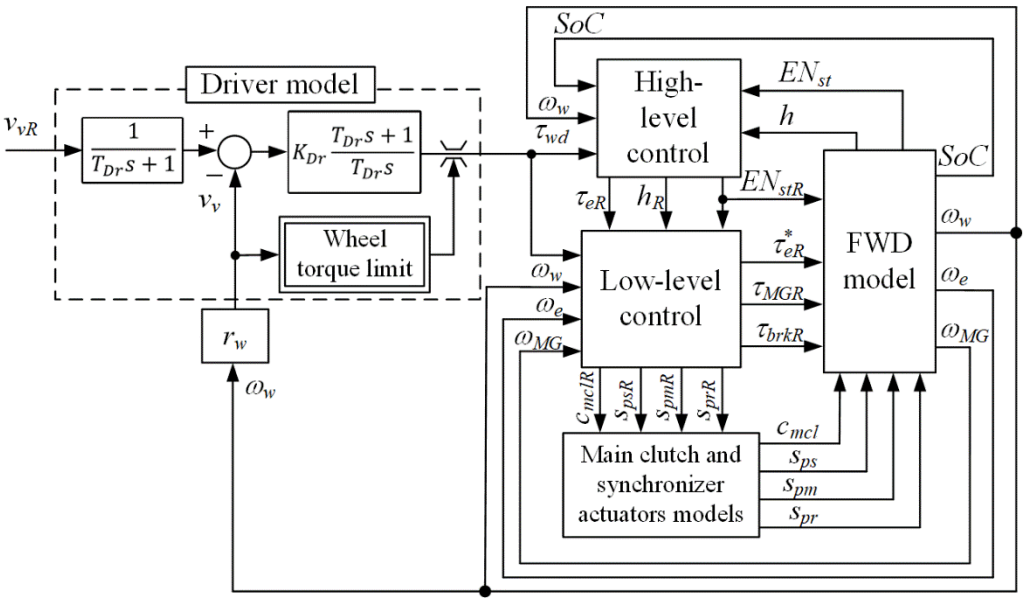

Figure 8. Block diagram of overall PHEV powertrain control system.

In the case of BWD model, the low-level controller and the driver submodel are omitted, because the powertrain dynamics are not accounted for, and the wheel speed and the torque demand are determined form the longitudinal dynamics given in Equations (1) and (2).

3.2. High-Level Control

The high-level control strategy combines a rule-based controller and an equivalent consumption minimization strategy (RB+ECMS control strategy; Figure 9, [5,23]). The rule-based strategy comprises a proportional-type SoC controller, engine start-stop logic, and powertrain kinematic equations for calculating the propulsion power demand P_d including the mechanical loss described within Equation (3). The SoC controller sets the battery power demand P^*_{batt} which is added to the propulsion power demand P_d to obtain the engine power demand P^*_e. The engine start/stop logic requests the engine to be switched on (EN_{stR} = 1) when the engine power demand P^*_e is greater than the engine-on power threshold P_{on} ($P^*_e > P_{on}$), and to be switched off (EN_{stR} = 0) if P^*_e is lower than engine-off power threshold P_{off} ($P^*_e \leq P_{off} < P_{on}$). Exceptionally, the engine will be kept switched on regardless of P^*_e if the M/G machine itself cannot deliver the power demand P_d due to its speed-dependent torque [5,23].

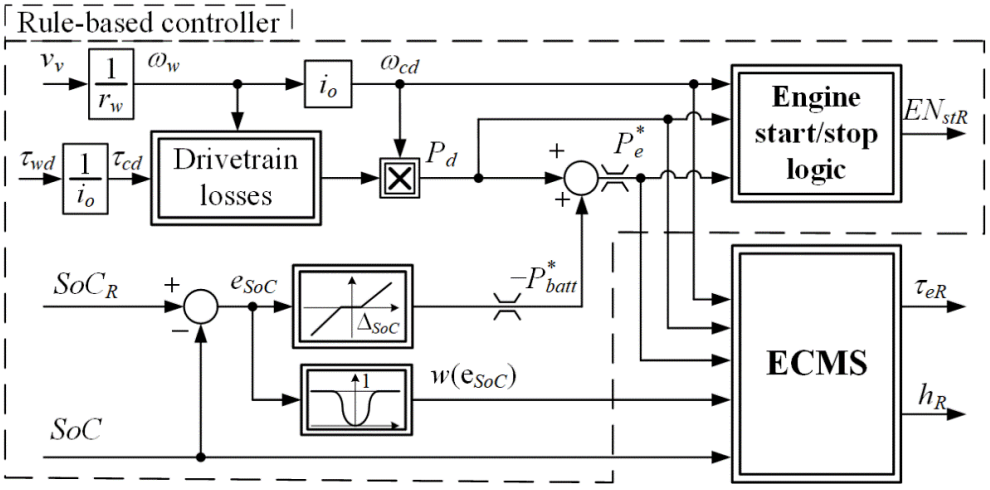

Figure 9. Block diagram of RB+ECMS-type high-level control strategy.

The ECMS instantaneously optimizes the engine torque and gear ratio references τ_{eR} and h_R to minimize the equivalent fuel consumption $\dot{m}_{eq}$ defined by [23]:

$$\min_{\tau_{eR,k}, h_{R,k}} \dot{m}_{eq,k} = \begin{cases} \dot{m}_{f,k} + A_{ek,k}\eta_{battc,k}P_{batt,k}, & \text{for } P_{batt,k} \le 0, \\ \dot{m}_{f,k} + \underbrace{\overline{A}_{ek}\eta_{battd,k}^{-1}P_{batt,k}}_{\dot{m}_{batt,k}}, & \text{for } P_{batt,k} > 0, \end{cases} \tag{8}$$

where the equivalent fuel consumption $\dot{m}_{eq}$ consists of the actual fuel mass flow $\dot{m}_f$ given by Equation (4) and the fuel equivalent $\dot{m}_{batt}$ of battery power. The symbols η_{battc} and η_{battd} denote the battery charging and discharging efficiencies, respectively, while $\overline{A}_{ek}$ is the mean engine specific fuel consumption accounting for engine efficiency during past battery charging periods [5,23]. The subscript k in Equation (8) stands for the discrete time step of control strategy execution, where the sampling time is equated with the BWD model sampling time T_d = 1 s (see Section 2). When calculating the quantities $\dot{m}_f$ and $\dot{m}_{batt}$ in Equation (8), the ECMS relies on the computationally efficient BWD model given by Equations (1)–(7).

The ECMS control variable search includes a SoC control error-dependent constraint on engine torque reference τ_{eR} [23]. Namely, the lower and upper engine torque reference limits vary between the absolute lower limit P_{off}/ω_e and the absolute upper limit $\tau_{e,\max}(\omega_e)$ depending on the SoC control error $e_{SoC} = SoC_R - SoC$, i.e., a smooth weighting function $w(e_{SoC})$. For $e_{SoC} = 0$, the limits are wide open, i.e., they correspond to the absolute limits. As e_{SoC} increases, the limits narrow and eventually converge to the operating point set by the RB controller $\tau_e = P^*_e/\omega_e$ at high values of e_{SoC}. In this way, the ECMS provides a 1D control variable search over the hyperbolic, constant power curve P^*_e = const. in the (ω_e, τ_e) plane if the SoC control error e_{SoC} is high, in order to respect the power demand P^*_e and suppress the SoC control error. On the other hand, if the control error e_{SoC} is low, the ECMS is allowed to give up from the power demand P^*_e and provides a 2D control variable search for reduced fuel consumption.

When the engine is switched off ($EN_{stR} = 0$, $\tau_{eR} = 0$), the M/G machine alone propels the vehicle and the transmission gear ratio is selected to minimize the total electric energy losses [23]:

$$h_{R,k} = \underset{h_{R,k}}{\operatorname{argmin}} \left(P_{batt,k} + I_{batt,k}^2 R(SoC_k) \right). \tag{9}$$

The RB+ECMS controller is supplemented with a gear shift delay algorithm (GSD) to reduce the number of gear switches by discouraging the ECMS to change the gear ratio too often [23]. This is achieved by extending the cost function (8) to

$$\dot{m}_{eq,k}(h_{R,k}) = r_f(t_{sh}, h_{k-1}, h_{R,k})\left(\dot{m}_f + \dot{m}_{batt}\right), \tag{10}$$

where a discount factor

$$r_f = \begin{cases} r_0 + t_{sh}\frac{1-r_0}{t_{th}}, & \text{for } t_{sh} < t_{th} \text{ and } h_{R,k} = h_{k-1}, \\ 1, & \text{otherwise}, \end{cases} \tag{11}$$

is introduced to shrink the cost if the ECMS search gear ratio candidate $h_{R,k}$ remains the same as the current gear $h_{k\text{-}1}$ and the time elapsed since the last gear shift, t_{sh}, is shorter than the time threshold t_{th}. The discount factor r_f varies from r_0 set to 0.6 and the nominal value of 1. The time threshold t_{th} is selected as a trade-off of powertrain efficiency and shift comfort (i.e., drivability). The discount factor r_f given by Equation (11) is also applied to the cost function given in Equation (9) related to the pure electric operating mode.

3.3. Low-Level Control

The low-level control strategy ensures realization of the engine torque reference τ_{eR} including the engine-on status reference EN_{stR}, the wheel torque demand τ_{wd}, and the gear ratio target h_R set by the high-level control strategy (Figure 8). This is achieved by coordinating the main clutch torque capacity reference c_{mclR}, the synchronizers s, m and r normalized position references s_{psR}, s_{pmR} and s_{prR}, respectively, the modified engine torque reference τ_{eR}, and the M/G machine torque reference τ_{MGR}. The low-level control operation is illustrated below for the following three characteristic powertrain transient modes: (i) engine-on switching, (ii) gear shifting while engine is switched on, and (iii) brake control. The low-level control strategy is implemented in C programing language within the Amesim model, with the sampling time set to 20 ms to capture the fast powertrain dynamics (e.g., those related to engine torque development).

3.3.1. Generation of M/G Machine and Mechanical Brake Torque References

When the main clutch is in open mode or transient state, the low-level control strategy resets the engine torque reference τ_{eR} to zero; otherwise, i.e., if the clutch is locked, $\tau_{eR} = \tau_{eR}$ holds. The M/G machine torque reference τ_{MGR} is determined as the difference between the wheel torque demand (τ_{wd}) referred to transmission input shaft and the modified engine torque reference τ_{eR}:

$$\tau_{MGR} = \frac{\tau_{wd}\eta_{tr}^{k_t}(\tau_{wd}) + \frac{P_0(\omega_w)}{\omega_w}}{i_o h} - \tau_{eR}^*. \tag{12}$$

Exceptionally, if the M/G machine torque τ_{MGR} is saturated during regenerative braking to its limit curve $\tau_{MG,\min}(\omega_{MG})$, the total (four-wheel) braking torque reference τ_{brkR} is set to fill the gap between the M/G machine reference and limit values, i.e., it is determined as the following:

$$\tau_{brkR} = \begin{cases} \tau_{wd}\eta_{tr}^{k_t}(\tau_{wd}) + \frac{P_0(\omega_w)}{\omega_w} - i_o h\tau_{MG,\min}(\omega_{MG}), & \text{for } \tau_{MGR} < \tau_{MG,min}(\omega_{MG}), \\ 0, & \text{otherwise.} \end{cases} \tag{13}$$

The engine torque reference τ_{eR} is reset to zero during braking intervals.

3.3.2. Low-Level Control for Engine-On Transient Mode

Low-level control for engine-on transient mode is segmented into three phases, as illustrated in Figure 10. In Phase 1, the main clutch is being engaged by means of open-loop

application of clutch torque capacity reference c_{mclR} which is determined assuming linearly falling clutch slip speed profile and prescribing the engagement time to Δt_{mcl} = 0.27s while considering the actuator dynamics with the time constant T_{mcl} (see Appendix B):

$$c_{mclR} = \frac{1}{\tau_{mcl,\max}} \frac{I_e |\omega_{mcl,start}|}{\left(T_{mcl} \left(1 - e^{-\frac{\Delta t_{mcl}}{T_{mcl}}} \right) - \Delta t_{mcl} \right)}, \tag{14}$$

where $\tau_{mcl,\max}$ is the maximum clutch torque capacity and $\omega_{mcl,start}$ is the initial clutch slip speed. The engine torque reference τ_{eR} is reset to zero and the M/G machine reference τ_{MGR} is set to deliver the driver-commanded wheel torque τ_{wd} (see Equation (12)).

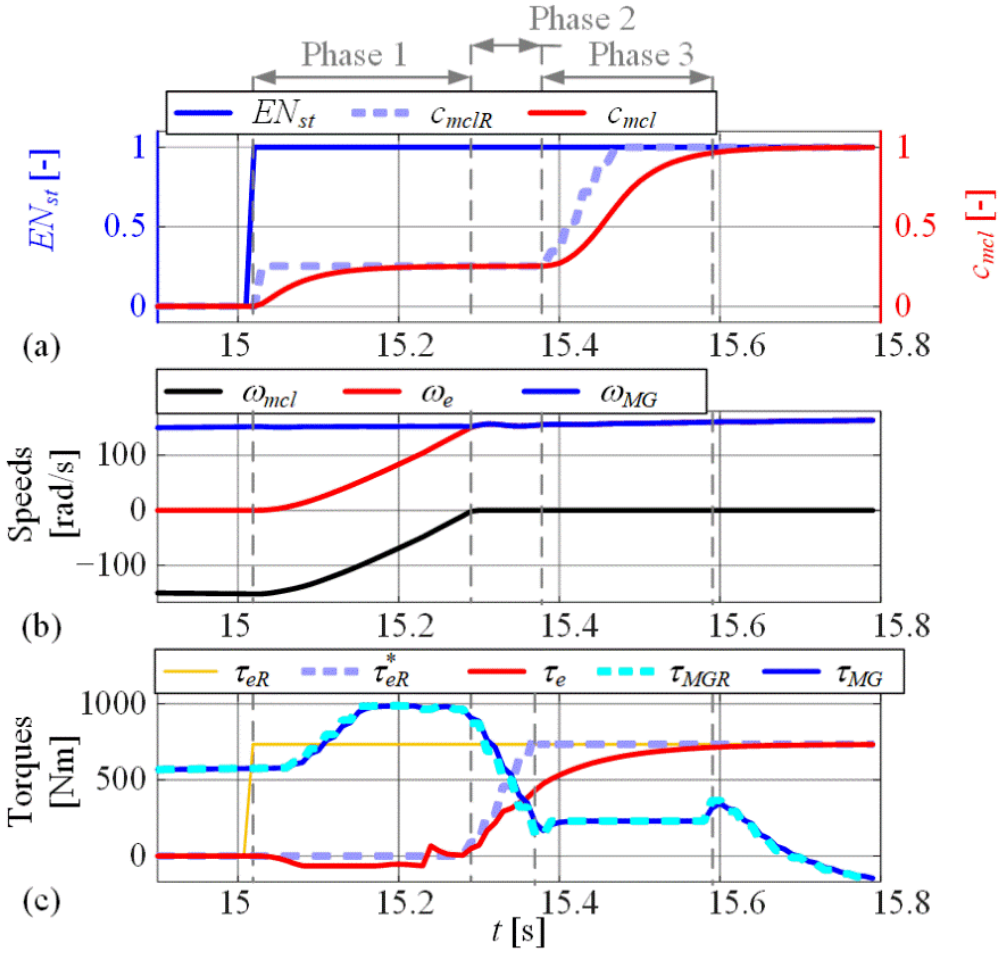

Figure 10. Low-level control system response during engine-on switching mode: engine status flag and main clutch normalized torque capacity (**a**), main clutch slip speed and engine and M/G machine speeds (**b**); engine and M/G machine reference and actual torques (**c**). Phases: (1) main clutch engagement, (2) engine torque buildup, (3) main clutch locking.

Phase 2 starts once the absolute value of clutch slip speed ω_{mcl} falls below a zero-speed threshold. In this phase, the engine torque reference τ^*_{eR} is linearly increased from zero to the reference τ_{eR} set by the high-level control strategy within the period of 0.1 s.

In the final stage (Phase 3), the clutch torque capacity reference c_{mclR} is linearly increased from the value determined by Equation (14) to the fully closed torque capacity value c_{mclR} = 1. Once the clutch is fully locked, i.e., when c_{mcl} = 1 is achieved, the transient mode is completed (see Figure 10a).

3.3.3. Low-Level Control during Gear Shifting

Low-level control during gear shifting is illustrated in Figure 11 for the case of 8–9 upshift, where the main (m) and splitter (s) gear stages change their states (see Table 1). The gear shifting is activated when the high-level control changes the gear reference h_R. In the engine-on case, the first gearshift phase (Phase 1 in Figure 11) starts with opening the main clutch by setting the clutch torque capacity and engine torque references to zero: $c_{mclR} = 0$ and $\tau_{eR} = 0$.

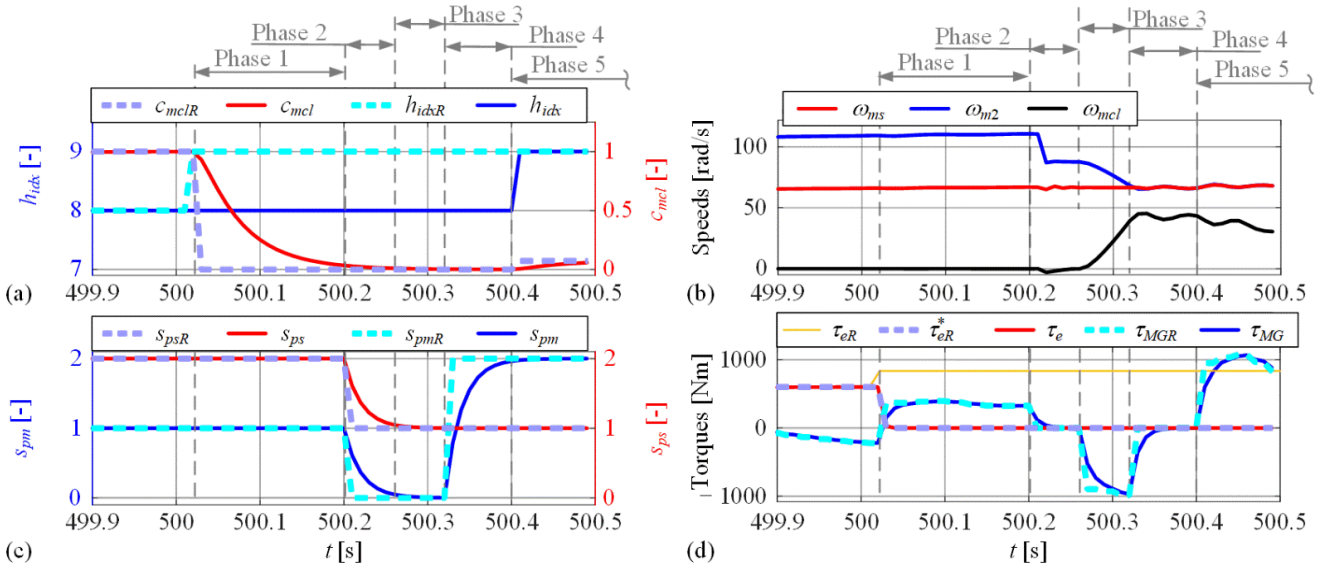

Figure 11. Low-level control system response during engine-on gear shifting mode (8–9 upshift): gear index and main clutch normalized torque capacity reference and actual responses (**a**), main clutch slip speed and main shaft and m_2 gear speeds (**b**), s-synchronizer and m-dog clutch reference and actual positions (**c**), engine and M/G machine reference and actual torques (**d**). Phases: (1) switching off engine and main clutch opening, (2) dog clutch opening and s-gear synchronization, (3) m-gear synchronization, (4) m-gear engagement, (5) M/G machine torque buildup.

Phase 2 starts once the main clutch is fully opened (Figure 11a). In this phase, the synchronizer s normalized position s_{ps} is commanded to change and synchronize the input shaft speed ω_{MG} with the counter shaft speed ω_{cs} and engaging the s-gear (s_1, Table 1). At the same time, the dog clutch m is commanded to be fully disengaged by setting its reference position s_{pmR} to zero. Phase 3 corresponds to synchronization of new m-gear (m_2, Table 1) with the main shaft speed ω_{ms}. The synchronization is performed by using a proportional-integral (PI) controller of the M/G machine speed ω_{MG}, with the reference ω_{MGR} set to reflect the synchronization speed ω_{ms}. The PI speed controller is tuned according to the damping optimum method [26], and its gains are scheduled to reflect the change of equivalent inertia when changing the gears. Note that Phase 3 is omitted for shifts that do not involve the change in m-gear.

Phase 4 starts when the new m-gear is synchronized, i.e., when the speed ω_{m2} approaches the speed ω_{ms} (Figure 10c). In this phase, the position reference s_{pmR} of synchronizer m is finally set to the value corresponding to gear m_2. Once the synchronizer position reference is reached (i.e., when s_{pm} approaches s_{pmR}), the target gear ratio h_R is set, and Phase 4 ends. For the sake of better visibility of the overall response in Figure 10, the response of fifth phase (Phase 5) covers only the initial interval of main clutch closing corresponding to Phase 1 in Figure 10. The remaining part of response is omitted as it is presented and discussed with Figure 10 as Phases 2 and 3. Note that for shifts where engine-off transition was commanded (i.e., if transition to electric mode occurred, $EN_{stR} = 0$) the main clutch would stay open, i.e., Phase 5 would be omitted. Similarly, in gear shifts occurring during pure electric operation, Phase 1 is omitted (see Figure 12).

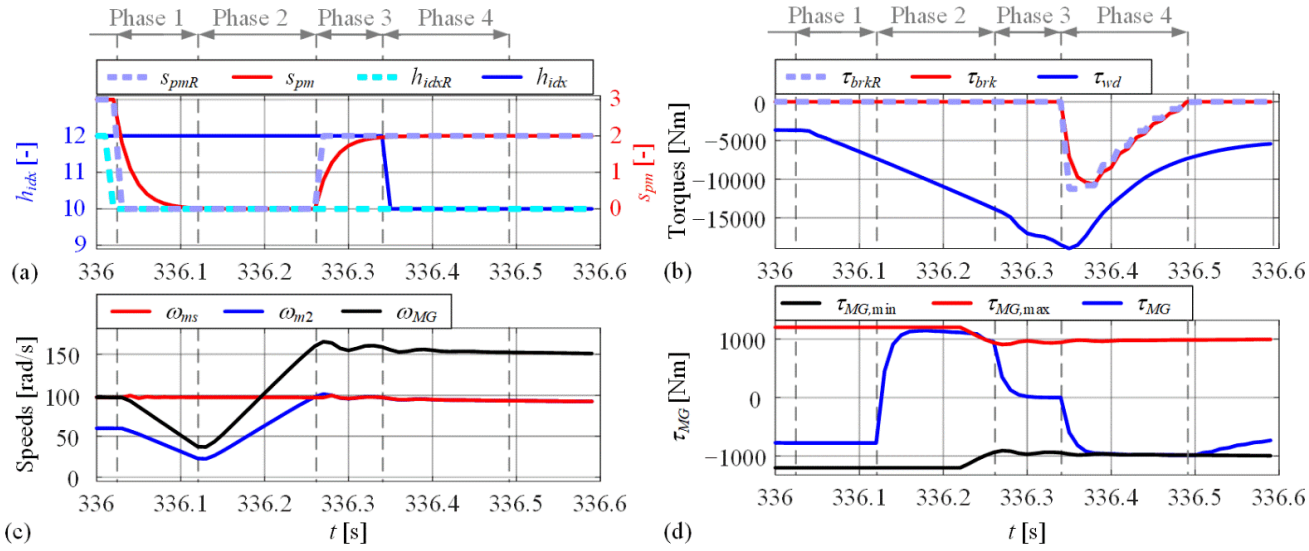

Figure 12. Low-level control system response during engine-off downshift transient including use of mechanical brakes (12-10 downshift): gear index and dog clutch position reference and actual responses (**a**), total wheel demand torque and reference and actual brake torque (**b**), main shaft, m_2 gear, and M/G machine speeds (**c**), M/G machine torque with corresponding limits (**d**). Phases: (1) dog clutch opening, (2) m-gear synchronization, (3) m-gear engagement, (4) M/G machine torque buildup and mechanical brake activation.

3.3.4. Low-Level Control during Braking Event

In the case of braking occurrence, the low-level control strategy fully relies on the M/G machine's regenerative braking torque, and it only activates the mechanical brakes τ_{brkR} if the braking torque demand $\tau_{wd} < 0$ exceeds the M/G machine torque limit $\tau_{MG,\min}$ (ω_{MG}) (Section 3.3.1). Low-level brake control is illustrated in Figure 12, where 12–10 downshift is commanded by the high-level control strategy during an interval of vehicle deceleration and pure electric operation ($EN_{st} = 0$). Before the downshift was commanded, the M/G machine regenerative braking torque τ_{MG} could fully meet the driver brake demand $\tau_{wd} < 0$ (see the initial period of response in Figure 12b), and the braking torque reference was set to zero ($\tau_{brkR} = 0$ Nm).

In Phase 1 of the downshift, the dog clutch m is commanded to be fully disengaged by setting its position to zero $s_{pmR} = 0$. Once the dog clutch 1 is fully opened, the downshift transfers to Phase 2, where the new m-gear (m_2, Table 1) is to be synchronized. Since the M/G machine is disconnected in this phase by the open dog clutch, the driver-demanded wheel braking torque $\tau_{wd} < 0$ is briefly not met. This results in increase of the vehicle velocity tracking error and consequent increase of absolute value of braking torque demand τ_{wd}. Once the new m-gear speed ω_{m2} is synchronized with main shaft speed ω_{ms} by means of closed-loop M/G machine control, Phase 3 starts, in which the dog clutch assumes its positions $s_{pm} = 2$ and the gear shift is completed. Although the mechanical brakes could have been used during Phases 1–3, the braking torque reference τ_{brkR} is deliberately set to zero ($\tau_{brkR} = 0$ Nm) to avoid energy dissipation on mechanical brakes and maximally utilize regenerative braking after the shift is completed (Phase 4 in Figure 12). Since the regenerative M/G machine torque $\tau_{MG} < 0$ becomes eventually saturated, the mechanical brake torque reference τ_{brkR} is determined according to Equation (13) to satisfy the braking torque demand $\tau_{wd} < 0$.

4. Extended Backward-Looking Powertrain Model

To maintain the computational efficiency of BWD model while increasing its accuracy towards that of the FWD model, an extended backward-looking model (EXT-BWD) is proposed in this section. The BWD model extension relates to capturing the power-

train transient effects, with emphasis on transient power losses. The model has physical background, where some of the dependencies/maps are created based on FWD model simulation responses.

4.1. Model Structure Overview

The structure of EXT-BWD model is outlined by the block diagram shown in Figure 13. As discussed in Section 3, the engine torque reference τ^*_{eR} is reduced to zero during the powertrain transients that involve manipulation of main clutch or dog clutches. During those intervals, the M/G machine predominantly delivers the traction power, and at the same time it covers additional transient-related losses such as the main clutch and synchronizers slippage losses, engine starting mechanical loss, and additional electrical loss related to M/G machine-based synchronization action for dog clutches.

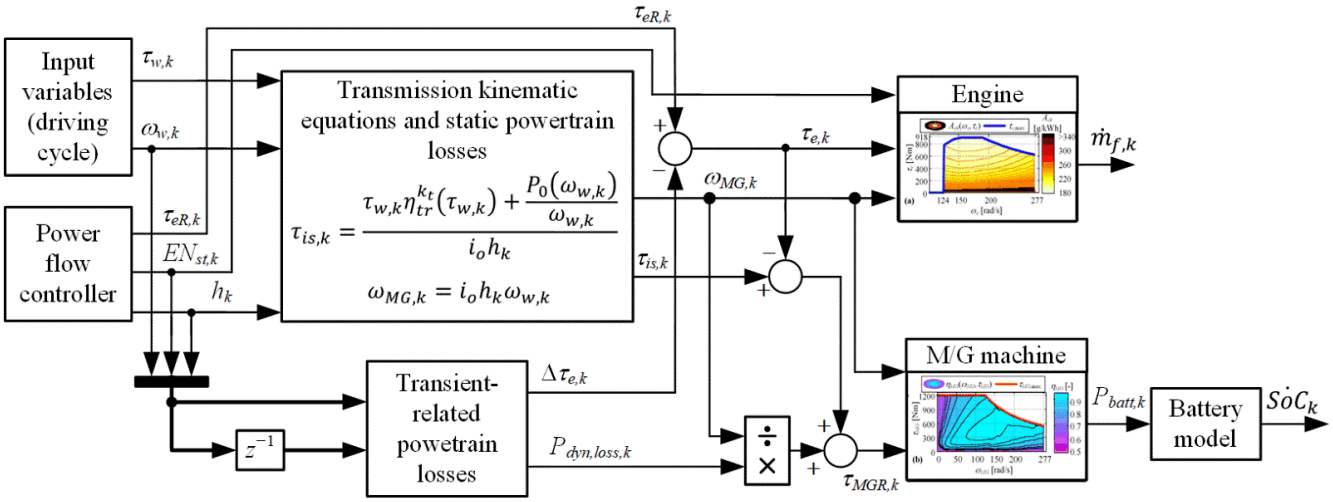

Figure 13. Block diagram of extended backward (EXT-BWD) model.

In the EXT-BWD model shown in Figure 13, the powertrain transient losses are accounted for through two static submodels that determine: (i) the equivalent engine torque loss $\Delta\tau_{e,k}$, and (ii) transient power losses $P_{dyn,loss}$. To calculate the torque and power losses, it turns out that it is necessary to know the engine on/off status in the previous sampling time ($EN_{st,k\text{-}1}$), the previous gear ratio ($h_{k\text{-}1}$), and the previous wheel/vehicle speed ($\omega_{w,k\text{-}1}$). To this end, the EXT-BWD model includes a one-step memory block $1/z$ for each of those three variables (Figure 13), as additional dynamic blocks to the battery model SoC integrator. The calculated engine torque cut $\Delta\tau_e$ is simply subtracted from the engine torque reference τ_{eR} to obtain the engine torque τ_e (Figure 13).

The transient power loss $P_{dyn,loss}$ is divided by the M/G machine speed ω_{MG} to obtain the corresponding torque loss, which is also added to the M/G machine torque reference to cover both static and dynamic torque losses (Figure 13). This calculation process is formally justified by the following M/G machine torque equation obtained by modifying the transmission input shaft torque balance Equation (3):

$$\tau_{MGR,k} = \underbrace{\frac{\tau_{w,k}\eta_{tr}^{k_t}(\tau_{w,k}) + \frac{P_0(\omega_{w,k})}{\omega_{w,k}}}{i_o h_k}}_{\tau_{is,k}} + \frac{P_{dyn,loss,k}}{\omega_{MG,k}} - \underbrace{\tau_{eR,k} + \Delta\tau_{e,k}}_{\tau_{e,k}}. \quad (15)$$

4.2. Engine Torque Loss

The engine torque loss $\Delta\tau_{e,k}$ from Figure 13 is defined as

$$\Delta\tau_{e,k} = r_c(EN_{st,k},\ EN_{st,k-1},\ h_k,\ h_{k-1})\tau_{eR,k},. \quad (16)$$

where $0 \leq r_c \leq 1$ is the engine torque reduction coefficient which is represented by a map (actually a table due to discrete amplitude inputs, see Appendix C) parameterized based on the results of exhaustive FWD model simulations. To extract the values of coefficient r_c, the engine torque reference commanded by the high-level control (τ_{eR}) is related to the delivered engine torque τ_e obtained from the forward model and averaged over the high-level controller sampling period T_d = 1 s ($\tau_{e,avg}$) as illustrated in Figure 14:

$$r_{c,k} = 1 - \frac{\tau_{e,avg,k}}{\tau_{eR,k}}. \tag{17}$$

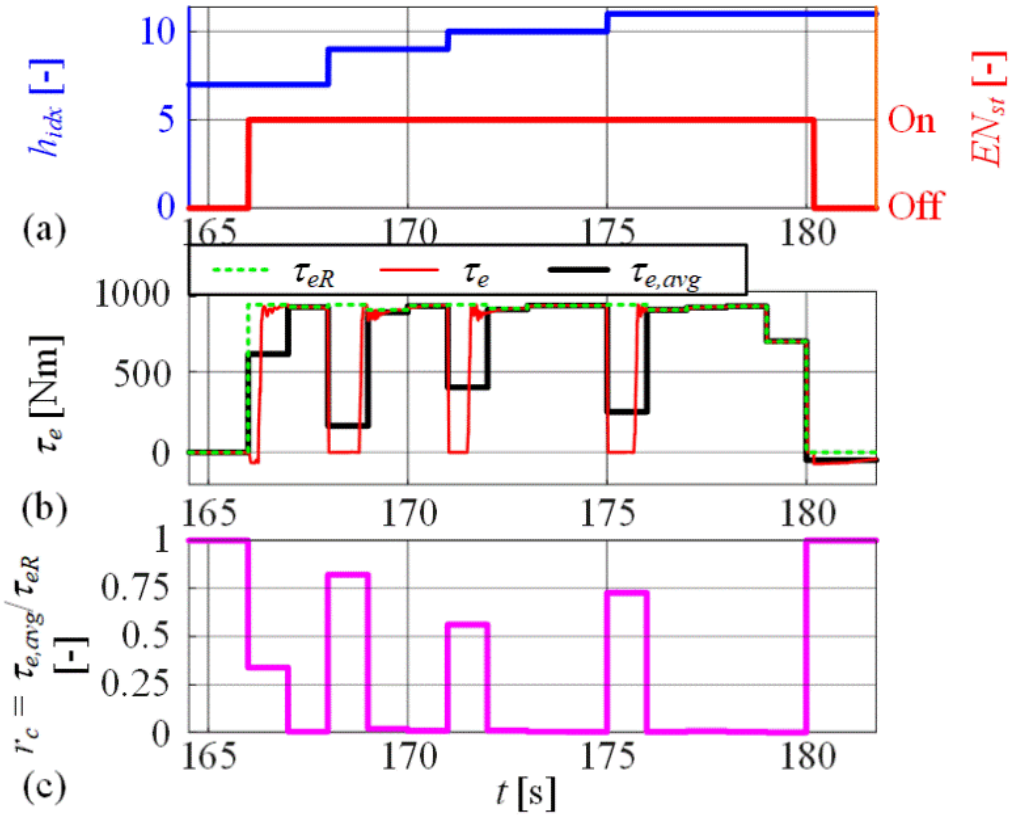

Figure 14. Illustration of identification of engine torque reduction coefficient r_c based on FWD model responses.

Mean values of $r_{c,k}$ calculated according to Equation (17) for different combinations of r_c-map inputs, which describe five distinct powertrain transient modes discussed in Appendix C, are stored in the engine torque reduction coefficient map $r_c(EN_{st,k}, EN_{st,k-1}, h_k, h_{k-1})$. In the special case of no engine status and shift transient, the coefficient r_c is set to zero, i.e., $\tau_e = \tau_{eR}$ applies as in the case of BWD model. If the engine is switched off, the coefficient r_c is set to 1, i.e., $\tau_e = 0$ holds.

4.3. Powertrain Transient Power Loss

The powertrain transient power loss $P_{dyn,loss}$ from Figure 13 is determined in each sampling instant $t_k = kT_d$ of the high-level control strategy (T_d = 1 s) from the following energy loss contributions: (i) main clutch and synchronizer slippage losses $E_{mcl,loss}$ and $E_{sync,loss}$, respectively, (ii) engine-on switching energy loss $E_{e,ON,loss}$, and (iii) M/G machine-based synchronization loss $E_{MG,sync}$:

$$P_{dyn,loss,k} = \frac{1}{T_d}\left(E_{mcl,loss,k} + E_{sync,loss,k} + E_{e,ON,loss,k} + E_{MG,sync,k}\right). \tag{18}$$

4.3.1. Main Clutch Slippage Energy Loss

Taking into account that during the main clutch engagement the engine torque reference is set to zero (τ_{eR^*}= 0 Nm; Figure 10) and the M/G machine speed is nearly constant ($\dot{\omega}_{MG} = 0$), the clutch slip speed dynamics can be described as:

$$\dot{\omega}_{mcl} = \dot{\omega}_e - \dot{\omega}_{MG} \cong \dot{\omega}_e = \frac{1}{I_e}(\tau_e - \tau_{mcl}) \cong -\frac{\tau_{mcl}}{I_e}, \tag{19}$$

where I_e is the engine inertia. Integrating Equation (19) while accounting for the initial condition $\omega_{mcl}(k) = \omega_{mcl,start}$ for the particular (k^{th}) sampling interval yields

$$E_{mcl,loss} = \int_0^{\Delta t_{mcl}} P_{mcl,loss}dt = \int_0^{\Delta t_{mcl}} \tau_{mcl}\omega_{mcl}dt \cong \int_0^{\Delta t_{mcl}} \tau_{mcl}\left(-\frac{\tau_{mcl}}{I_e}t + \omega_{mcl,start}\right)dt, \tag{20}$$

where Δt_{mcl} is the target clutch engagement time (see Equation (14)). Based on the assumption that $\dot{\omega}_{MG} = 0$, the initial clutch slip speed may be expressed as

$$\omega_{mcl,start} \cong \omega_{e,k} - \omega_{e,k-1}. \tag{21}$$

For the constant clutch torque capacity reference c_{mclR}, taking into account the actuator dynamics, the main clutch torque τ_{mcl} during the engagement period can be expressed as

$$\tau_{mcl} = \tau_{mcl,\max}c_{mcl} = \tau_{mcl,\max}c_{mclR}\left(1 - e^{-\frac{t}{T_{mcl}}}\right). \tag{22}$$

Inserting Equation (22) into Equation (20), accounting for Equation (21), solving the integral Equation (20) and rearranging gives the following final expression for the main clutch energy loss:

$$E_{mcl,loss,k} = \begin{cases} k_{mcl}\omega_{mcl,start}^2, & \text{for } (EN_{st,k} = 1 \text{ i } EN_{st,k-1} = 0) \\ & \text{or } (EN_{st,k} = 1 \text{ i } h_k \neq h_{k-1}), \\ 0, & \text{otherwise,} \end{cases}, \tag{23}$$

with the coefficient k_{mcl} given by

$$k_{mcl} = I_e\left(-\frac{1}{2c_{mcl}^2}\left(T_{mcl}^2 b_{mcl} + T_{sync}^2 + 4T_{mcl}^2 a_{mcl} - 2T_{mcl}T_{sync}a_{mcl}\right) - 1\right), \tag{24}$$

where the expressions for coefficients a_{mcl}, b_{mcl} and c_{mcl} are included in Appendix A.

4.3.2. Synchronizer Slippage Energy Loss

The total synchronizer slippage energy loss is expressed as the following:

$$E_{sync,loss,k} = \sum_i \sum_j E_{s,i,j,loss,k}, \tag{25}$$

where $i \in$ [s, r] and $j \in$ [1,2] stand for the synchronizer stage and the ordinal number of the synchronizer within the stage, respectively (see Figure 2). In order to facilitate analytical derivation, the following assumptions are made: (i) the synchronizer actuator dynamics have negligible influence, (ii) only the synchronizer s engages during the gear shift (i.e., synchronizers m and r stay locked), and (iii) the counter-shaft has a nearly constant speed ($\dot{\omega}_{cs} = 0$) due to the high output inertia, which gives:

$$E_{s,s,j,loss,k} = \frac{1}{2}I_{MG1}\omega_{ss,k-1}^2 = \frac{1}{2}I_{MG1}(i_o h_k \omega_{w,k} - i_o h_{k-1}\omega_{w,k-1})^2, \tag{26}$$

where I_{MG1} is the lumped M/G machine and input shaft inertia. Note that the synchronizer s slip speed $\omega_{ss,k}$ in k^{th} step (i.e., after the transient) equals to zero ($\omega_{ss,k} = \omega_{MG,k} - \omega_{cs,k} = 0$ rad/s), and by assuming near constant counter shaft speed ω_{cs} ($\dot{\omega}_{cs} = 0$, $\omega_{cs,k} = \omega_{cs,k-1}$) the slip speed at the start of the transient $\omega_{ss,k-1}$ equals to difference of M/G machine speed prior and after the transient ($\omega_{ss,k-1} = \omega_{MG,k-1} - \omega_{MG,k}$, see Equations (26) and (2)). Similarly, assuming the constant output shaft speed during the r-gear synchronization ($\dot{\omega}_{os} = 0$), negligible influence of synchronizer actuator dynamics, and inactive s- and m-gears, the r-gear synchronization loss is given by

$$E_{s,r,j,loss,k} = \frac{1}{2} I_{MG2} \omega_{sr,k-1}^2 = \frac{1}{2} I_{MG2} (i_o h_{r,k} \omega_{w,k} - i_o h_{r,k-1} \omega_{w,k-1})^2, \tag{27}$$

where I_{MG2} is the lumped M/G machine, input, counter, and main shaft inertia, h_r is the h-gear speed ratio of the engaged r-gear, and $\omega_{sr,k-1}$ is the synchronizer r slip speed before the gear shift transient, where, similarly to the case of synchronizer s, the slip speed $\omega_{sr,k-1}$ equals to the difference of main shaft prior and after the transient ($\omega_{sr,k-1} = \omega_{ms,k-1} - \omega_{ms,k}$).

4.3.3. M/G Machine-Based Synchronization Energy Loss

The M/G machine-based synchronization loss of m-gear dog clutch is expressed as

$$E_{MG,sync,k} = \frac{1}{2} I_{MG3} \left(\omega_{MG,k}^2 - \omega_{MG,k-1}^2 \right), \tag{28}$$

where I_{MG3} is the lumped M/G machine, input and counter-shaft inertia.

4.3.4. Engine-On Energy Losses While Switching On

The engine-start loss $E_{e,ON,loss}$ includes the loss related to change in engine kinetic energy $E_{e,kin,loss}$ and the engine drag-related loss $E_{drag,loss}$:

$$E_{e,ON,loss,k} = E_{e,kin,loss} + E_{drag,loss} = \frac{I_e \omega_{e,idle}^2}{2} + \int_0^{\Delta t_{idle}} \omega_e(t) \tau_{e,drag}(\omega_e) dt, \tag{29}$$

where $\omega_{e,idle}$ is the engine idle speed, $\tau_{e,drag}$ is the engine drag torque (see Figure 7a), and Δt_{idle} is the average time of reaching the idle speed, which is calculated from a rich set of FWD model responses. The integral in Equation (29) is numerically and off-line solved based on the assumption of constant engine acceleration (equal to $\omega_{e,idle}/\Delta t_{idle}$, Section 3), and the resulting constant engine-on energy loss is applied on-line, i.e., when evaluating the model.

4.3.5. Inertial Load of Powertrain Components

Finally, for improved accuracy of the EXT-BWD model, the equivalent mass of rotating powertrain components is determined as the following (see Figures 5 and 6):

$$m_{add} = \frac{2I_w + (I_e + I_{MG} + I_{cs} + I_{ms} + I_{os}) \hat{h}^2 i_o^2}{r_w^2}, \tag{30}$$

where $\hat{h}$ is the transmission gear ratio obtained offline as a shift scheduling map fed by the wheel speed and wheel torque demand inputs. The shift scheduling map is obtained by minimizing the pure electric drive cost function given in Equation (9). The equivalent mass given by Equation (30) is added to the vehicle mass M_v within the longitudinal dynamics Equation (1).

4.3.6. Use of EXT-BWD Model within ECMS+RB Control Strategy

In order to improve the control performance, the RB+ECMS control strategy is modified to rely on the EXT-BWD model shown in Figure 13, and it is denoted as RB+ECMS-EXT. Although the EXT-BWD model is somewhat more complex than the original BWD model, the RB+ECMS-EXT strategy still executes as comparably fast as in the case of its RB+ECMS counterpart.

The GSD algorithm described by Equations (10) and (11) represents a heuristic method of reducing the number of gear shifts and improving drivability when applying the RB+ECMS control strategy. Since the RB+ECMS-EXT strategy inherently accounts for the shift-related transient energy losses, it naturally avoids frequent shifting, and it does not require the GSD algorithm (i.e., it is omitted in the RB+ECMS-EXT strategy).

5. Dynamic Programming-Based Control Variable Optimization and EXT-BWD Model Validation

5.1. Optimal Problem Formulation

DP algorithm can provide globally optimal solution when solving a general non-convex control variable optimization problem [27,28]. The DP-based optimization is computationally feasible only for problems with a low number of control and state variables, which is the case with backward-type PHEV models [28,29]. The resolution of state and control variable quantization is selected as a trade-off between optimization accuracy and execution time. In the case of BWD model, the battery SoC is the only state variable $x_k = SoC_k$ (see Section 2). In the case of EXT-BWD model, the state variable SoC_k is supplemented by the engine on/off status and the gear ratio variables in the previous, $(k-1)^{\text{st}}$ step, which are designated as $EN_{st,prev,k}$ and $h_{prev,k}$, respectively (see Figure 13 and note that the third signal for which the memory block z^{-1} is applied therein is not a state, but rather an external input ω_w, which is known in advance):

$$\mathbf{x}_k = \begin{bmatrix} SoC_k & EN_{st,prev,k} & h_{prev,k} \end{bmatrix}^T. \tag{31}$$

In both backward model variants, the engine torque reference $\tau_{eR,k}$ and the transmission gear ratio h_k are set as elements of the control input vector

$$\mathbf{u}_k = \begin{bmatrix} \tau_{eR,k} & h_k \end{bmatrix}^T. \tag{32}$$

The wheel torque demand $\tau_{w,k}$ and the current wheel speed $\omega_{w,k}$, as well as the previous wheel speed $\omega_{w,k\text{-}1}$ in the case of EXT-BWD model, are combined into the external input vector

$$\mathbf{v}_k = \begin{bmatrix} \tau_{w,k} & \omega_{w,k} & \omega_{w,k-1} \end{bmatrix}^T. \tag{33}$$

The EXT-BWD model state-space system includes the SoC dynamics given by Equation (6) and discretized in time by using the Euler forward method with T_d = 1 s, as well as the following one-step delay state equations for the additional states $EN_{st,prev,k}$ and $h_{prev,k}$:

$$\begin{bmatrix} EN_{st,prev,k+1} \\ h_{prev,k+1} \end{bmatrix} = \begin{bmatrix} 0 & 0 \\ 0 & 0 \end{bmatrix} \begin{bmatrix} EN_{st,prev,k} \\ h_{prev,k} \end{bmatrix} + \begin{bmatrix} f_{EN,st}(\cdot) & 0 \\ 0 & 1 \end{bmatrix} \begin{bmatrix} \tau_{e,k} \\ h_k \end{bmatrix}, \tag{34}$$

where $f_{EN,st}(u)$ is the step-type activation function, which equals 1 if $u > 0$, while it is set to 0 if $u \leq 0$. The overall discrete-time state-space system is described in the following vector form:

$$\mathbf{x}_{k+1} = f(\mathbf{x}_k, \mathbf{u}_k, \mathbf{v}_k) \tag{35}$$

with the initial and final conditions given by

$$\mathbf{x}_i = \begin{bmatrix} SoC_i & EN_{st,prev,i} & h_{prev,i} \end{bmatrix}^T, , \tag{36}$$

$$\mathbf{x}_f = \begin{bmatrix} SoC_f & EN_{st,prev,f} & h_{prev,f} \end{bmatrix}^T. \tag{37}$$

The cumulative discrete cost function J to be minimized by the DP algorithm is defined as

$$J = J_f + \sum_{k=0}^{N-1} F(x_k, u_k, v_k), \tag{38}$$

with the cost to go function F specified as

$$\begin{aligned} F(x_k, \mathbf{u}_k, \mathbf{v}_k) = {} & T_d \dot{m}_{f,k} + \\ & + K_g \left\{ H^-(x_k - SoC_{\min}) + H^-(SoC_{\max} - x_k) \right\} \\ & + K_g \left\{ H^-(P_{batt}^{\max} - P_{batt,k}) + H^- \left(P_{batt,k} - P_{batt}^{\min} \right) \right\} \\ & + K_g \left\{ H^- \left(\mathbf{u}_k - \mathbf{u}_k^{\min} \right) + H^-(\mathbf{u}_k - \mathbf{u}_k^{\max}) \right\} \\ & + K_g \left\{ H^- \left(\omega_{e,k} - \omega_e^{\min} \right) + H^-(\omega_e^{\max} - \omega_{e,k}) \right\} \\ & + K_g \left\{ H^- \left(\tau_{MG,k} - \tau_{MG}^{\min} \right) + H^-(\tau_{MG}^{\max} - \tau_{MG,k}) \right\} \\ & + K_g \left\{ H^- \left(\omega_{MG,k} - \omega_{MG}^{\min} \right) + H^-(\omega_{MG}^{\max} - \omega_{MG,k}) \right\}, \end{aligned} \tag{39}$$

where the first right-hand side term represents the fuel consumption increment while the remaining terms stand for inequality constraints related to the physical limits of various variables [28]. The inverted Heaviside function $H^-(x)$ is defined as $H^-(x) = 1$ for $x < 0$, and $H^-(x) = 0$ otherwise. The penalization factor K_g is set to a sufficiently high value (10^{12}, herein) to ensure that constraints are satisfied.

The final condition penalization term

$$J_f = \begin{bmatrix} K_f & 0 & 0 \end{bmatrix} \left(\mathbf{x}_f - f(\mathbf{x}_{N-1}, \mathbf{u}_{N-1}, \mathbf{v}_{N-1}) \right)^2 \tag{40}$$

is introduced in Equation (38) to satisfy that $SoC(t_f)$ is equal to the final condition SoC_f, where the weighting factor is set to $K_f = 10^6$.

The DP algorithm is implemented in C++ programming language to improve the computational efficiency. The previous gear ratio and engine on/off status states h_{k-1} and $EN_{st,k-1}$, respectively, are inherently discrete variables, and have only 2 and 12 discrete levels, respectively. The gear ratio control input h_k has 12 discrete levels, while the battery SoC state SoC_k and the engine torque control input $\tau_{e,Rk}$ are originally continuous variables and are discretized into 200 levels each.

5.2. Optimization Results

DP-based control variable optimization has been carried out for the case of charge-sustaining (CS) mode, where $SoC_i = SoC_f = 30\%$, and three heavy-duty certification driving cycles (HDUDS, WHVC and JE05) and a recorded city bus driving cycle with the road grade set to zero (denoted as DUB; [30]). The optimization results obtained for both BWD and EXT-BWD models are given in Table 2. They include the total fuel consumption V_f and the related final SoC value $SoC(t_f)$ as well as the number of gear shifts N_g and engine-on switching N_e. In the case of realistic DUB driving cycle, the fuel consumption predicted by EXT-BWD model is 9% higher than that predicted by BWD model. This indicates that the BWD model is largely optimistic in predicting the fuel consumption because of neglected transient losses. Furthermore, the number of gear shifts N_g and engine-on events N_e is approximately halved in the case of EXT-BWD model when compared to BWD model. This is because the transient events are discouraged when accounting for the transient losses within the EXT-BWD model. In the case of artificial/certification driving cycles, the fuel consumption predicted by the EXT-BWD model is around 5% higher than that of the

BWD model, while the level of drivability improvement is comparable to that of DUB cycle (around 50% less shifting/switching events).

Table 2. DP-based control variable optimization results for different driving cycles and two types of BWD model.

Cycle	Model	V_f [L]	$SoC(t_f)$ [%]	N_e [-]	N_g [-]
DUB	**BWD**	**1.80** (+0.0%)	**29.75** (+0.0%)	**64** (+0.0%)	**967** (+0.0%)
	EXT-BWD	1.96 (+8.9%)	29.76 (+0.0%)	28 (−56.3%)	555 (−42,6%)
HDUDDS	**BWD**	**2.02** (+0.0%)	**29.74** (+0.0%)	**25** (+0.0%)	**168** (+0.0%)
	EXT-BWD	2.12 (+5.0%)	29.89 (+0.5%)	13 (−48.0%)	92 (−45.0%)
WHVC	**BWD**	**4.22** (+0.0%)	**29.85** (+0.0%)	**51** (+0.0%)	**365** (+0.0%)
	EXT-BWD	4.40 (+4.3%)	29.69 (−0.5%)	26 (−49.0%)	190 (−47.9%)
JE05	**BWD**	**2.54** (+0.0%)	**29.80** (+0.0%)	**54** (+0.0%)	**466** (+0.0%)
	EXT-BWD	2.66 (+4.7%)	29.61 (−0.6%)	22 (−59.3%)	224 (−51.9%)

5.3. Validation of EXT-BWD Model

For the purpose of EXT-BWD model validation, the DP-optimized control variables obtained for the EXT-BWD model and the BWD model, $\mathbf{u}_{EXT\text{-}BWD}$ and $\mathbf{u}_{BWD}$, are fed to the original, more accurate FWD model in an open-loop manner. The fuel consumption and SoC trajectories predicted by the EXT-BWD, BWD, and FWD models, and given in travelled distance x-axis, are shown in Figure 15 for the four driving cycles considered in Table 2. These results show that, when applying the input $\mathbf{u}_{EXT\text{-}BWD}$, the EXT-BWD and FWD models predict very similar SoC and fuel consumption trajectories where the final values match within the error margin of 1.5%. On the other hand, when applying the input $\mathbf{u}_{BWD}$ to BWD and FWD model, the fuel consumption and SoC trajectories of the two models deviate substantially, especially for more dynamic (and realistic) DUB driving cycles. The BWD model-predicted final fuel consumption and SoC are underestimated to a large extent (at least −10% offset for $SoC(t_f)$ and 30% reduced V_f). This is, again, due to neglected transient losses in the case of BWD model.

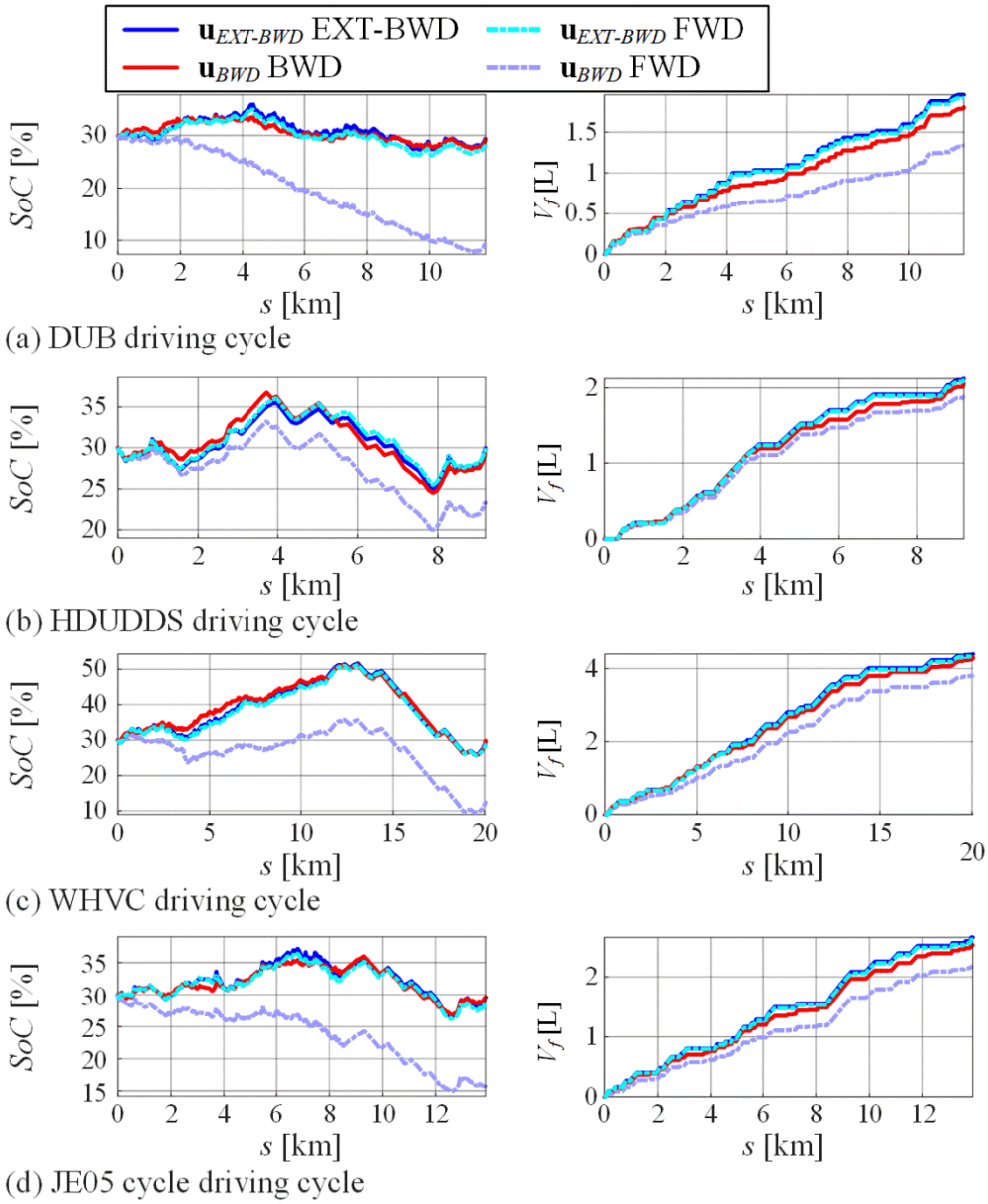

Figure 15. SoC and fuel consumption trajectories given over travelled distance and predicted by BWD, EXT-BWD, and FWD models fed by DP-optimized control variables of BWD and EXT-BWD models for DUB (**a**), HDUDDS (**b**), WHVC (**c**) and JE05 (**d**) driving cycles.

6. Control System Simulation Results

The control strategies based on BWD and EXT-BWD models, which are referred to as RB+ECMS and RB+ECMS-EXT, are verified and compared in this section. Applying these strategies to the EXT-BWD model produces the results shown in Table 3, where those related to RB+ECMS correspond to two cases: with and without gear shift delay (GSD) algorithm. The results include relative differences of the control system performance indicators with respect to those of DP optimal results (see the values given in parentheses). To provide consistent comparison in the presence of floating final SoC values $SoC(t_f)$ in the case of control system, the DP optimizations have been conducted for a number of final SoC conditions SoC_f around the target of 30%. The respective optimal fuel consumption values V^*_f are linearly interpolated with respect to final SoC conditions SoC_f, and as such they are used to calculate the indicators' relative differences.

Table 3. Comparative simulation results for control strategies based on BWD and EXT-BWD models (denoted as RB+ECMS and RB+ECMS-EXT, respectively) when applied to EXT-BWD model.

Strategy	V_f [L]	$SoC(t_f)$ [%]	N_e [-]	N_g [-]
DUB driving cycle				
RB+ECMS, w/o GSD	2.11 (+9.0%)	28.91	48	696 (0.0%)
RB+ECMS, w/GSD	2.10 (+8.7%)	28.93	48	383 (−45.0%)
RB+ECMS-EXT	2.04 (+5.2%)	28.95	45	371 (−46.7%)
HDUDDS driving cycle				
RB+ECMS, w/o GSD	2.33 (+3.2%)	32.99	11	167 (0.0%)
RB+ECMS, w/GSD	2.34 (+3.4%)	33.14	11	88 (−47.3%)
RB+ECMS-EXT	2.31 (+2.1%)	33.12	12	79 (−52.7%)
WHVC driving cycle				
RB+ECMS, w/o GSD	4.64 (+3.8%)	31.35	21	327 (0.0%)
RB+ECMS, w/GSD	4.63 (+3.7%)	31.35	22	187 (−42.8%)
RB+ECMS-EXT	4.61 (+3.1%)	31.38	22	188 (−42.5%)
JE05 driving cycle				
RB+ECMS, w/o GSD	2.72 (+4.6%)	28.15	24	480 (0.0%)
RB+ECMS, w/GSD	2.72 (+4.6%)	28.18	24	220 (−54.2%)
RB+ECMS-EXT	2.68 (+3.0%)	28.24	24	236 (−50.8%)

The performance indicators shown in Table 3 point out that the use of GSD algorithm within RB+ECMS results in significant reduction (≅50%) of the number of gear shifts N_g for all driving cycles. At the same time, the fuel consumption is mostly improved, but only marginally. On the other hand, RB+ECMS-EXT considerably reduces the fuel consumption relative excess with respect to DP benchmark (see the percentage values in V_f column). The reduction is most significant in the case of realistic DUB driving cycle where the fuel consumption excess is reduced from 8.7% to 5.2%. RB+ECMS-EXT has comparable number of gear shifts N_g to that of RB+ECMS with GSD algorithm included. This is achieved through physical description of transient losses rather than using a heuristic GSD algorithm. The number of engine-on switching N_e is comparable for all control strategies considered.

The performance comparison of RB+ECMS w/GSD and RB+ECMS-EXT when applied to more accurate FWD model is presented in Table 4. For the sake of consistent comparison, the total fuel consumption V_f is corrected with respect to deviation of final SoC from its target value SoC_R = 0.3:

$$V_{f,corr} = V_f + \Delta V_f \left(SoC\left(t_f\right) - SoC_R \right), \tag{41}$$

where the sensitivity parameter ΔV_f is obtained by forming a linear regression of multiple $SoC(t_f)$ vs. V_f pairs obtained by a series of simulations with different values SoC_R [5]. The results in Table 4 point out that RB+ECMS-EXT outperforms RB+ECMS in terms of fuel consumption, and the extent of improvement is similar as in the case (EXT)-BWD model simulations (cf. Table 3). In the most realistic case of DUB driving cycle, the fuel consumption reduction is 2.2%, which is achieved by computationally non-demanding extension of RB+ECMS.

Table 4. Strategies based on BWD and EXT-BWD models (denoted as RB+ECMS and RB+ECMS-EXT, respectively) when applied to FWD model.

Strategy	V_f [L]	$V_{f,corr}$ [L]	$SoC(t_f)$ [%]	N_e [-]	N_g [-]
DUB driving cycle					
RB+ECMS, w/GSD	2.13	2.28 (0.0%)	27.78	61	499 (0.0%)
RB+ECMS-EXT	2.16	2.23 (−2.2%)	28.45	59	452 (−9.4%)
HDUDDS driving cycle					
RB+ECMS, w/GSD	2.29	2.18 (0.0%)	32.60	17	97 (0.0%)
RB+ECMS-EXT	2.30	2.16 (−0.9%)	33.46	12	106 (+9.3%)
WHVC driving cycle					
RB+ECMS, w/GSD	4.68	4.56 (0.0%)	33.07	22	288 (0.0%)
RB+ECMS-EXT	4.73	4.53 (−0.7%)	34.79	29	266 (−7.6%)
JE05 driving cycle					
RB+ECMS, w/GSD	2.71	2.79 (0.0%)	28.07	22	239 (0.0%)
RB+ECMS-EXT	2.84	2.77 (−0.7%)	31.68	25	253 (−5.9%)

7. Conclusions

In this paper, a detailed forward-looking (FWD) powertrain model has been proposed for a plug-in hybrid electric vehicle (PHEV) given in P2 parallel configuration. The FWD model includes a low-level control system built around 12-speed automated manual transmission shift controls. Furthermore, an extended backward-looking (EXT-BWD) model has been proposed to account for the powertrain torque and power losses during engine-on and transmission shift events. The EXT-BWD model shares the advantages of FWD model (accuracy) and conventional BWD model (computational efficiency).

The dynamic programming (DP)-based PHEV control variable optimization algorithm has been extended to reflect the structure of EXT-BWD model. The extended DP optimization algorithm has been employed for validating the EXT-BWD model, where the DP-optimal control variables were fed into the EXT-BWD and FWD models for comparison of fuel consumption and battery state of charge (SoC) trajectories. The validation results have shown that the EXT-BWD model predicts final SoC and fuel consumption values that approach those obtained by the FWD model with the relative error margins lower than 1.5%, which is by an order of magnitude lower than what can be achieved by using the conventional BWD model.

The previously developed, combined rule-based and equivalent consumption minimization strategy (RB+ECMS)-type high-level controller has been extended to account for

the engine-on and gear shifting transient losses described by the EXT-BWD model. The extended control strategy, denoted as RB+ECMS-EXT, outperforms RB+ECMS when applied to both EXT-BWD and FWD models. The improvement is most pronounced for a realistic dynamic driving cycle of considered city bus vehicle, and it is reflected in 2.2% lower fuel consumption as well as mostly reduced number of gear shifts (by 5–10%). These performance gains are achieved without any significant reduction of computational efficiency.

The future work will focus on extending the RB+ECMS-EXT control strategy with a control parameters adaptation law. In addition, model predictive control based on the EXT-BWD model will be considered.

Author Contributions: Conceptualization, J.S., J.D.; methodology, J.S., I.C., J.D.; software, J.S., I.C.; validation, J.S., I.C.; writing—original draft preparation, J.S.; writing—review and editing, J.D., I.C; supervision: J.D. All authors have read and agreed to the published version of the manuscript.

Funding: It is gratefully acknowledged that this work has been supported by the Croatian Science Foundation under the project No. IP-2018-01-8323 (Project Acronym: ACHIEVE; web site: http://achieve.fsb.hr/, accessed on 8 September 2022).

Institutional Review Board Statement: Not applicable.

Informed Consent Statement: Not applicable.

Conflicts of Interest: The authors declare no conflict of interest.

Appendix A: Powertrain and Control Strategy Parameters

The values of PHEV model parameters are: M_v = 12.635 kg, R_0 = 0.012, i_o = 4.72, r_w = 0.481 m, C_d = 0.7, ρ_{air} = 1.225 g/m^3, A_f = 7.52 m^2, $Q_{\max}$ = 30 Ah.

The values of RB+ECMS controller parameters are: P_{on} = 80 kW, P_{off} = 30 kW, $\overline{A}_{ek}$= 195 g/kWh, K_{SoC} = 736,000 W, Δ_{SoC} = 0.02.

The expressions for coefficients of Equation (24) read:

$$a_{mcl} = 1 - e^{-\frac{\Delta t_{mcl}}{T_{mcl}}}, \quad b_{mcl} = 1 - e^{-\frac{2\Delta t_{mcl}}{T_{mcl}}}, \quad c_{mcl} = T_{mcl} a_{mcl} - \Delta t_{mcl}.$$

Appendix B: Generating Main Clutch Normalized Torque Capacity Reference

By combining Equations (19) and (22), the main clutch slip speed dynamics can be written as

$$\dot{\omega}_{mcl} = -\frac{\tau_{mcl}}{I_e} = -\frac{\tau_{mcl,\max} c_{mcl}}{I_e} = -\frac{\tau_{mcl,\max} c_{mclR}}{I_e}\left(1 - e^{-\frac{t}{T_{mcl}}}\right). \tag{A1}$$

By integrating the Equation A1 from t= 0 s to $t = \Delta t_{mcl}$ and considering the boundary conditions $\omega_{mcl}(\Delta t_{mcl}) = 0$ rad/s and $\omega_{mcl}(0) = \omega_{mcl,start}$, the following equality applies:

$$\omega_{mcl,start} = \frac{\tau_{mcl,\max}}{I_e}\left(T_{mcl}\left(1 - e^{-\frac{\Delta t_{mcl}}{T_{mcl}}}\right) - \Delta t_{mcl}\right) c_{mclR}, \tag{A2}$$

from which Equation (14) is derived.

Appendix C: Engine Torque REDUCTION Coefficient

The engine torque reduction coefficient r_c is identified for five distinct powertrain transient modes, which include: (i) engine-on transient with no gear shifting, (ii) and (iii) engine-on and gear shift transient with and without m-gear change, respectively, and (iv) and (v) gear shift transient only with and without m-gear change, respectively. The transient mode is determined based on the gear ratio h and the engine on/off status EN_{st} in the current k^{th} and previous $(k-1)^{\text{st}}$ steps.

The engine torque reduction coefficient values identified for the five transient modes based on FWD model simulations are given in Figure A1. These values are used to

determine the mean r_c for each transient mode, which is then stored in the map $r_c(EN_{st,k}, EN_{st,k-1}, h_k, h_{k-1})$ depending on the transient mode input obtained for the four map inputs.

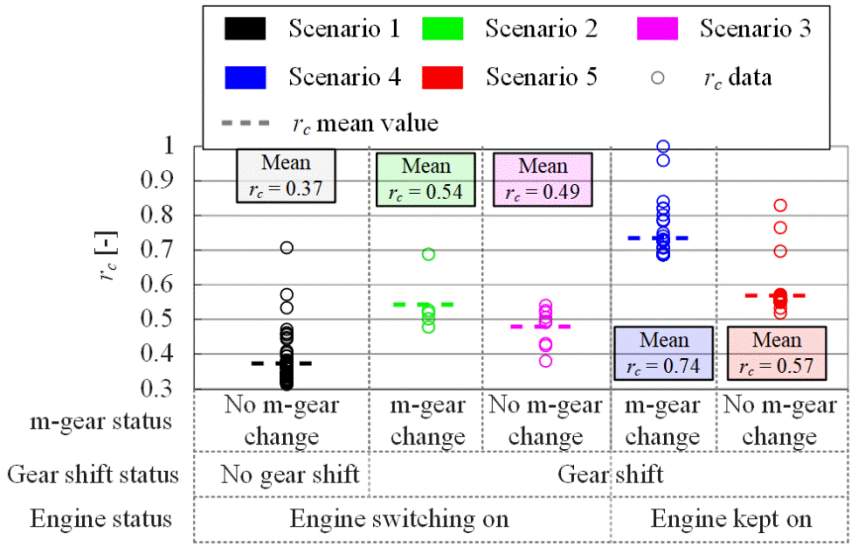

Figure A1. Engine torque reduction coefficient for five characteristic powertrain transient modes.

References

1. Martinez, C.M.; Hu, X.; Cao, D.; Velenis, E.; Gao, B.; Wellers, M. Energy Management in Plug-in Hybrid Electric Vehicles: Recent Progress and a Connected Vehicles Perspective. *IEEE Trans. Veh. Technol.* **2017**, *66*, 4534–4549. [CrossRef]
2. Ouddah, N.; Adouane, L. Hybrid Energy Management Strategy Based on Fuzzy Logic and Optimal Control for Tri-Actuated Powertrain System. *IEEE Trans. Veh. Technol.* **2019**, *68*, 5343–5355. [CrossRef]
3. Lee, W.; Jeoung, H.; Park, D.; Kim, N. An Adaptive Concept of PMP-Based Control for Saving Operating Costs of Extended-Range Electric Vehicles. *IEEE Trans. Veh. Technol.* **2019**, *68*, 11505–11512. [CrossRef]
4. Enang, W.; Bannister, C. Robust proportional ECMS control of a parallel hybrid electric vehicle. *Proc. Inst. Mech. Eng. Part D J. Automob. Eng.* **2017**, *231*, 99–119. [CrossRef]
5. Škugor, B.; Deur, J.; Cipek, M.; Pavković, D. Design of a power-split hybrid electric vehicle control system utilizing a rule-based controller and an equivalent consumption minimization strategy. *Proc. Inst. Mech. Eng. Part D J. Automob. Eng.* **2014**, *228*, 631–648. [CrossRef]
6. Guzzella, L.; Sciaretta, A. *Vehicle Propulsion Systems*, 2nd ed.; Springer: Berlin/Heidelberg, Germany, 2007.
7. Schmid, R.; Buerger, J.; Bajcinca, N. Energy Management Strategy for Plug-in-Hybrid Electric Vehicles Based on Predictive PMP. *IEEE Trans. Control Syst. Technol.* **2021**, *29*, 2548–2560. [CrossRef]
8. Chen, D.; Kim, Y.; Stefanopoulou, A.G. Predictive Equivalent Consumption Minimization Strategy with Segmented Traffic Information. *IEEE Trans. Veh. Technol.* **2020**, *69*, 14377–14390. [CrossRef]
9. Opila, D.F.; Wang, X.; McGee, R.; Gillespie, R.B.; Cook, J.A.; Grizzle, J.W. Real-world robustness for hybrid vehicle optimal energy management strategies incorporating drivability metrics. *J. Dyn. Syst. Meas. Control Trans. ASME* **2014**, *136*, 061011. [CrossRef]
10. Soldo, J.; Cvok, I.; Deur, J. Bond Graph-Based Energy Balance Analysis of Forward and Backward Looking Models of Parallel Plug-In Hybrid Electric Vehicle. *SAE Tech. Pap.* **2022**, *1*, 743.
11. Galvagno, E.; Guercioni, G.; Rizzoni, G. Effect of Engine Start and Clutch Slip Losses on the Energy Management Problem of a Hybrid DCT Powertrain. *Int.J. Automot. Technol.* **2020**, *21*, 953–969. [CrossRef]
12. Opila, D.F.; Wang, X.; McGee, R.; Gillespie, R.B.; Cook, J.A.; Grizzle, J.W. An energy management controller to optimally trade off fuel economy and drivability for hybrid vehicles. *IEEE Trans. Control Syst. Technol.* **2012**, *20*, 1490–1505. [CrossRef]
13. Tota, A.; Galvagno, E.; Dimauro, L.; Vigliani, A.; Velardocchia, M. Energy management strategy for hybrid multimode powertrains: Influence of inertial properties and road inclination. *Appl. Sci.* **2021**, *11*, 11752. [CrossRef]
14. Škugor, B.; Ranogajec, V.; Deur, J. On smoothing HEV/EREV supervisory control action using an extended ECMS approach. In Proceedings of the 2013 World Electric Vehicle Symposium and Exhibition (EVS27), Barcelona, Spain, 17–20 November 2013; IEEE: Piscataway, NJ, USA.
15. Yakhshilikova, G.; Ruzimov, S.; Ezemobi, E.; Tonoli, A.; Amati, N. Development of Optimization Based Control Strategy for P2 Hybrid Electric Vehicle including Transient Characteristics of Engine. *Appl. Sci.* **2022**, *12*, 2852. [CrossRef]
16. Kim, S.; Choi, S.B. Cooperative Control of Drive Motor and Clutch for Gear Shift of Hybrid Electric Vehicles with Dual-Clutch Transmission. *IEEE/ASME Trans. Mechatron.* **2020**, *25*, 1578–1588. [CrossRef]
17. Yan, F.; Wang, J.; Huang, K. Hybrid electric vehicle model predictive control torque-split strategy incorporating engine transient characteristics. *IEEE Trans. Veh. Technol.* **2012**, *61*, 2458–2467. [CrossRef]

18. Ganesan, A.; Gros, S.; Murgovski, N.; Lee, C.F.; Sivertsson, M. Effect of engine dynamics on optimal power-split control strategies in hybrid electric vehicles. In Proceedings of the 2020 IEEE Vehicle Power and Propulsion Conference (VPPC), Gijon, Spain, 18 November–16 December 2020.
19. Bidarvatan, M.; Shahbakhti, M. Analysis and control of torque split in hybrid electric vehicles by incorporating powertrain dynamics. *J. Dyn. Syst. Meas. Control. Trans. ASME* **2018**, *140*, 111009. [CrossRef]
20. Chen, R.; Zou, Y.; Hou, S. Heuristic Dynamic Programming Based Online Energy Management Strategy for Plug-In Hybrid Electric Vehicles. *IEEE Trans. Veh. Technol.* **2019**, *68*, 843–851.
21. Guercioni, G.R.; Galvagno, E.; Tota, A.; Vigliani, A. Adaptive equivalent consumption minimization strategy with rule-based gear selection for the energy management of hybrid electric vehicles equipped with dual clutch transmissions. *IEEE Access* **2020**, *8*, 190017–190038. [CrossRef]
22. Volvo 7900 Electric Hybrid Specifications. Available online: https://www.volvobuses.co.uk/en-gb/our-offering/buses/volvo-7900-electric-hybrid/specifications.html (accessed on 17 March 2021).
23. Soldo, J.; Škugor, B.; Deur, J. Optimal energy management and shift scheduling control of a parallel plug-in hybrid electric vehicle. *Int. J. Powertrains* **2020**, *9*, 240–264. [CrossRef]
24. Siemens. *Simcenter Amesim 2020.1: Integration Algorithms Used in Simcenter Amesim*; Technical Bulletin No. 102; Siemens: Munich, Germany, 2020.
25. Pacejka, H.B. *Tire and Vehicle Dynamics*, 3rd ed.; Elsevier: Amsterdam, The Netherlands, 2012.
26. Deur, J.; Pavković, D. Fundamentals of electrical drive controls. In *Electrical Engineering—Fundamentals of Electrical Drive Controls*; EOLSS Publishers: Oxford, UK, 2011; pp. 1–59.
27. Bellman, R.E.; Dreyfus, S.E. *Applied Dynamic Programming*; Princeton University Press: Princeton, NJ, USA, 1962.
28. Soldo, J.; Škugor, B.; Deur, J. Analysis of optimal battery state-of-charge trajectory patterns for blended mode of a parallel plug-in hybrid electric vehicle and a wide range of driving conditions. *Optim. Eng.* **2021**, *22*, 1955–1977. [CrossRef]
29. Cipek, M.; Škugor, B.; Čorić, M.; Kasać, J.; Deur, J. Control variable optimisation for an extended range electric vehicle. *Int. J. Powertrains* **2016**, *5*, 30–54. [CrossRef]
30. Škugor, B.; Hrgetić, M.; Deur, J. GPS measurement-based road grade reconstruction with application to electric vehicle simulation and analysis. In Proceedings of the 11th Conference on Sustainable Development of Energy, Water and Environment Systems (SDEWES 2015), Dubrovnik, Croatia, 27 September–2 October 2015.